Analysis of von Kármán's swirling flow on a rotating disc in Bingham fluids

Abhijit Guha and Sayantan Sengupta

Citation: Physics of Fluids **28**, 013601 (2016); doi: 10.1063/1.4937590
View online: http://dx.doi.org/10.1063/1.4937590
View Table of Contents: http://scitation.aip.org/content/aip/journal/pof2/28/1?ver=pdfcov
Published by the AIP Publishing

Articles you may be interested in

Thin-liquid-film flow on a topographically patterned rotating cylinder
Phys. Fluids **26**, 042102 (2014); 10.1063/1.4869208

Suppression of purely elastic instabilities in the torsional flow of viscoelastic fluid past a soft solid
Phys. Fluids **25**, 124102 (2013); 10.1063/1.4840195

Mixed convection flow of viscoelastic fluid over a sphere with constant heat flux
AIP Conf. Proc. **1522**, 453 (2013); 10.1063/1.4801161

Two regimes of self-propelled motion of a torus rotating about its centerline in a viscous incompressible fluid at intermediate Reynolds numbers
Phys. Fluids **24**, 053603 (2012); 10.1063/1.4717760

Fluctuation of magnetic induction in von Kármán swirling flows
Phys. Fluids **18**, 085105 (2006); 10.1063/1.2265009

This article is copyrighted as indicated in the article. Reuse of AIP content is subject to the terms at: http://scitation.aip.org/termsconditions. Downloaded to IP: 203.110.246.23 On: Sun, 10 Jan 2016 14:27:14

CrossMark click for updates

PHYSICS OF FLUIDS **28**, 013601 (2016)

Analysis of von Kármán's swirling flow on a rotating disc in Bingham fluids

Abhijit Guha[a] and Sayantan Sengupta[b]
Mechanical Engineering Department, Indian Institute of Technology Kharagpur, Kharagpur 721302, India

(Received 8 February 2015; accepted 13 November 2015; published online 6 January 2016)

In this article, the flow above a rotating disc, which was first studied by von Kármán for a Newtonian fluid, has been investigated for a Bingham fluid in three complementary but separate ways: by computational fluid dynamics (CFD), by a semi-analytical approach based on a new transformation law, and by another semi-analytical approach based on von Kármán's transformation. The full equations, which consist of a set of partial differential equations, are solved by CFD simulations. The semi-analytical approach, in which a set of ordinary differential equations is solved, is developed here by simplifying the full equations invoking several assumptions. It is shown that the new transformation law performs better and reduces to von Kármán's transformation as a limiting case. The present paper provides a closed-form expression for predicting the non-dimensional moment coefficient which works well in comparison with values obtained by the full CFD simulations. Detailed variations of tangential, axial, and radial components of the velocity field as a function of Reynolds number (Re) and Bingham number (Bn) have been determined. Many subtle flow physics and fluid dynamic issues are explored and critically explained for the first time in this paper. It is shown how two opposing forces, viz., the viscous and the inertial forces, determine certain important characteristics of the axial-profiles of non-dimensional radial velocity (e.g., the decrease of maxima, the shift of maxima, and the crossing over). It has been found that, at any Re, the maximum value of the magnitude of non-dimensional axial velocity decreases with an increase in Bn, thereby decreasing the net radial outflow. A comparison between the streamline patterns in Newtonian and Bingham fluids shows that, for a Bingham fluid, a streamline close to the disc-surface makes a higher number of complete turns around the axis of rotation. The differences between the self-similarity in a Newtonian fluid flow and the non-similarity in a Bingham fluid flow are expounded with the help of a few compelling visual representations. Some major differences and similarities between the flow of a Newtonian fluid above a rotating disc and that of a Bingham fluid, deduced in the present investigation, are brought together in a single table for ready reference. Two limiting cases, viz. $Bn \to 0$ and $Re \to \infty$, are considered. The present results show that the Bingham fluid solution progressively approaches the von Kármán's solution for a Newtonian fluid as the Bingham number is progressively reduced to zero ($Bn \to 0$). It is also established here that, for finite values of Bn, the Bingham fluid solution progressively approaches the von Kármán's solution for a Newtonian fluid as the non-dimensional radius and Reynolds number increase. The higher the value of Bn, the higher is the required value of Re at which convergence with the solution for Newtonian fluid occurs. © *2016 AIP Publishing LLC*. [http://dx.doi.org/10.1063/1.4937590]

[a]Electronic mail: a.guha@mech.iitkgp.ernet.in
[b]Author to whom correspondence should be addressed. Electronic mail: sayantansengupta@iitkgp.ac.in

 ©2016 AIP Publishing LLC

This article is copyrighted as indicated in the article. Reuse of AIP content is subject to the terms at: http://scitation.aip.org/termsconditions. Downloaded to IP: 203.110.246.23 On: Sun, 10 Jan 2016 14:27:14

I. INTRODUCTION

The fluid dynamics of the flow above a rotating disc has been a topic of extensive research for nearly a century. Other than its fundamental importance, the study of such flow is relevant for many engineering devices such as turbomachinery or computer storage devices and for many engineering applications such as spin-coating, lubrication and fabrication of computer memory. The pioneering paper[1] in this field was written by the great fluid dynamicist Theodore von Kármán. For steady, laminar, and incompressible flow of a Newtonian fluid, von Kármán had given a similarity solution considering infinite expanse of the fluid on either side of a rotating disc. The physical process through which von Kármán's steady flow field arises may be understood in the following way. Initially, the fluid is stationary everywhere. As the rotating disc imparts rotational motion to the quiescent fluid due to the no slip boundary condition, a boundary layer is developed near the rotating disc. Inside the boundary layer, the fluid is pumped radially outward due to the effect of centrifugal force. For this radial flow to sustain, the fluid flows axially towards the disc satisfying the equation of continuity. Therefore, the velocity vectors inside the boundary layer have tangential, radial, and axial components. The process of generating a steady radial efflux of the fluid is known as the free disc pumping effect.[2]

After von Kármán, many researchers contributed in this field yielding various perspectives. A comprehensive review containing some major investigations (up to 1987) on the flow of a Newtonian fluid above a rotating disc is available in Ref. 3. Some of the recent developments in this research-area can be found in Refs. 4–8. The effects of externally supplied mass flux on the flow above a rotating disc can be found in Refs. 9–12. A description of the contribution of famous fluid dynamicists like Batchelor,[13] Ekman,[14] and Stewartson,[15] and, a good survey of related work on rotational boundary layer in Newtonian fluids are provided by Guha and Sengupta.[11] Researchers have also extended von Kármán's investigation to various non-Newtonian fluids. Berman and Pasch[16] experimentally investigated von Kármán's flow in a polymer solution. Acrivos *et al.*,[17] Andersson *et al.*,[18] Ming *et al.*,[19] etc. investigated von Kármán's flow in a power-law fluid. Siddiqui *et al.*[20] studied von Kármán's flow in a Jeffrey fluid. Detailed studies on von Kármán's flow in a viscoelastic fluid can be found in Refs. 21–23. However, the corresponding fluid dynamics in a viscoplastic fluid has not been studied to any great extent. The present work therefore aims to fill this gap by presenting a rigorous and thorough study of the von Kármán's swirling flow in an important category of viscoplastic fluid.

A viscoplastic fluid is a non-Newtonian fluid which evinces a threshold value of stress, known as the yield stress. A viscoplastic fluid flows only when the applied stress exceeds the yield stress of the fluid. Below the yield stress, a viscoplastic fluid behaves like a solid. Muds and clays, slurries and suspensions, heavy oils, avalanches, cosmetic creams, hair gel, hand cream, liquid chocolate, crystallizing lavas, certain polymer solutions, and some pastes are a few examples of viscoplastic fluid.[24,25] Balmforth *et al.*[26] have shown the importance of the study of viscoplastic fluids to understand various processes and applications in the natural and engineering sciences. An important category of viscoplastic fluids is known as the Bingham fluid which obeys the Bingham model.[27] The model is very popular for explaining the behaviour of many fluids exhibiting the yield-stress phenomena.

The flow of a Bingham fluid over a rotating disc has attracted some attention in the recent past. The mass transfer aspect in such flow has been investigated in Ref. 28 and a semi-analytical approach for predicting von Kármán's flow in a Bingham fluid, using von Kármán's similarity transformation for a Newtonian fluid, is presented in Ref. 29. In the present paper, a rigorous and comprehensive analysis is presented on von Kármán's swirling flow in a Bingham fluid. Two complementary approaches have been developed—a semi-analytical formulation based on a newly proposed transformation and computational fluid dynamic (CFD) simulations. Many subtle and complex aspects of the flow-field have been revealed and discussed using both approaches. It is shown how the new transformation reduces to von Kármán's transformation as a limiting case, and how the new solutions for a Bingham fluid reduce to the solutions for a Newtonian fluid in the limit of zero Bingham number or infinitely large Reynolds number.

This article is copyrighted as indicated in the article. Reuse of AIP content is subject to the terms at: http://scitation.aip.org/termsconditions. Downloaded to IP: 203.110.246.23 On: Sun, 10 Jan 2016 14:27:14

It is believed that the paper contains the first CFD solutions for the flow of a Bingham fluid above a rotating disc. The present CFD method is not restricted by some of the assumptions that are considered for the development of the semi-analytical technique. Hence, the CFD method seems to be more generic as compared to the semi-analytical technique. However, the semi-analytical technique provides a set of ordinary differential equations (ODEs) by which it is easier to analyse von Kármán's swirling flow in a Bingham fluid. Therefore, the first objective of the present work is to obtain rigorous and thorough solutions of the von Kármán's swirling flow in a Bingham fluid, using both analytical and computational methods. The second objective of the present study is to provide new fluid dynamic understanding that is developed in course of the present investigation. It has been shown here that von Kármán's swirling flow in a Bingham fluid exhibits non-similarity. Typical shapes of boundary layer surfaces for various Bingham numbers due to the non-similar velocity distributions are shown for the first time in this article. The Newtonian limits (when either $Bn \to 0$ or $Re \to \infty$) for the rotational boundary layer solutions in a Bingham fluid are introduced in this paper. Some subtle fluid dynamic aspects for von Kármán's swirling flow in a Bingham fluid have been critically explained.

II. MATHEMATICAL FORMULATION

In this section, the governing differential equations for the flow of a Bingham fluid above a rotating disc are provided. The equations are expressed in a cylindrical coordinate system. Figure 1(a) shows a schematic of a rotating disc and a cylindrical coordinate system. r (radial), θ (azimuthal), and z (axial) are the three coordinates and o is the origin of the cylindrical coordinate system. The surface of the disc is located at $z = 0$ and, invoking symmetry, the solutions given in this paper are for $z \geq 0$.

In the present study, the flow is considered to be steady, axi-symmetric, laminar, incompressible, and isothermal. Navier-Stokes equations in the cylindrical coordinate system under these flow-conditions[30] are as follows:

$$\frac{\partial V_r}{\partial r} + \frac{V_r}{r} + \frac{\partial V_z}{\partial z} = 0, \tag{1}$$

$$\rho\left(V_r\frac{\partial V_r}{\partial r} - \frac{V_\theta^2}{r} + V_z\frac{\partial V_r}{\partial z}\right) = -\frac{\partial p}{\partial r} + \frac{\partial \tau_{zr}}{\partial z} + \frac{\partial \tau_{rr}}{\partial r} + \frac{\tau_{rr} - \tau_{\theta\theta}}{r}, \tag{2}$$

$$\rho\left(V_r\frac{\partial V_\theta}{\partial r} + \frac{V_r V_\theta}{r} + V_z\frac{\partial V_\theta}{\partial z}\right) = \frac{1}{r^2}\frac{\partial}{\partial r}\left(r^2\tau_{r\theta}\right) + \frac{\partial \tau_{z\theta}}{\partial z}, \tag{3}$$

$$\rho\left(V_r\frac{\partial V_z}{\partial r} + V_z\frac{\partial V_z}{\partial z}\right) = -\frac{\partial p}{\partial z} + \frac{1}{r}\frac{\partial}{\partial r}\left(r\tau_{rz}\right) + \frac{\partial \tau_{zz}}{\partial z}. \tag{4}$$

Equations (1)–(4) contain the partial derivatives of absolute tangential velocity V_θ, absolute radial velocity V_r, absolute axial velocity V_z, pressure p, and components of stress tensor τ_{ij}.

The boundary conditions for obtaining von Kármán's solutions[31] are as follows:

$$\text{at } z = 0, \quad V_r = 0, \ V_\theta = r\Omega, \text{ and } V_z = 0 \tag{5}$$

$$\text{as } z \to \infty, \quad V_r \to 0, \ \text{ and } V_\theta \to 0. \tag{6}$$

In Equation (5), Ω denotes the rotational speed of a disc at a steady state.

The governing Equations (1)–(4) and the boundary conditions (5)-(6) are applicable for Newtonian as well as non-Newtonian fluids. The difference between the various types of fluids is reflected in the expressions of the elements of the stress tensor τ_{ij} in Equations (2)–(4). von Kármán's original solution was obtained for a Newtonian fluid. In the present work, we want to develop a similar analysis for a specific type of non-Newtonian fluid, viz. the Bingham fluid. The constitutive relation for a Bingham fluid flow[32] is given as follows:

$$\begin{aligned} \tau_{ij} &= \left(\tau_y/\dot{\gamma} + \mu_p\right) e_{ij} = \eta(\dot{\gamma})\, e_{ij}, \qquad \text{for } \tau > \tau_y, \\ e_{ij} &= 0, \qquad\qquad\qquad\qquad\quad \text{for } \tau \leq \tau_y, \end{aligned} \tag{7}$$

This article is copyrighted as indicated in the article. Reuse of AIP content is subject to the terms at: http://scitation.aip.org/termsconditions. Downloaded to IP: 203.110.246.23 On: Sun, 10 Jan 2016 14:27:14

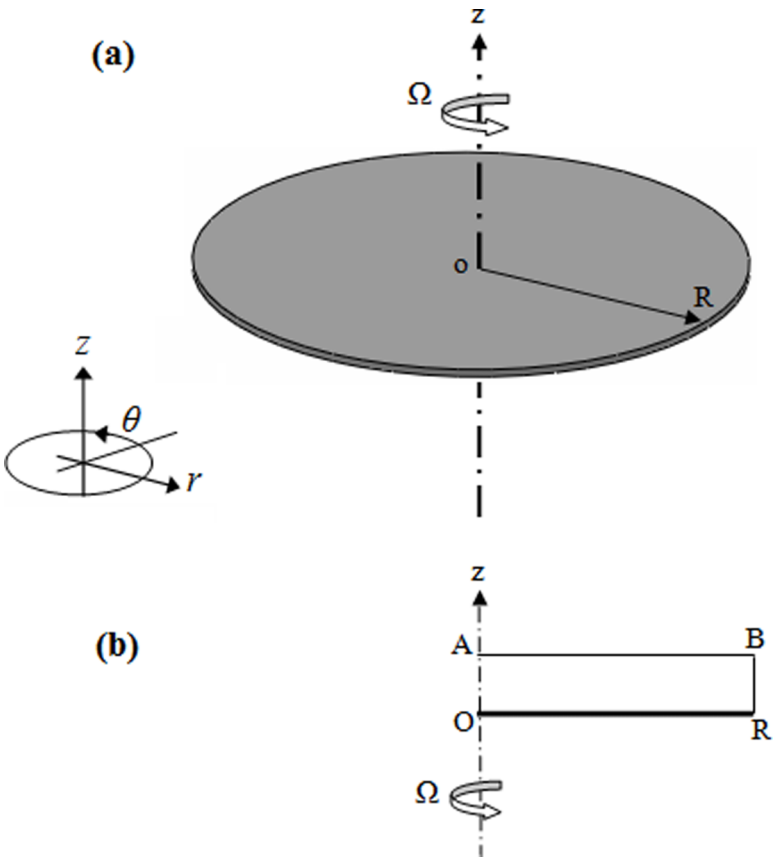

FIG. 1. Schematic diagram of a rotating disc and the computational flow domain. (a) A rotating disc and the cylindrical coordinates; (b) a two-dimensional computational domain (ORBA) which is used to determine a three-dimensional, axi-symmetric flow field. OR is the disc-surface, RB represents the ambient fluid at the edge of the disc, BA represents the ambient fluid at the top of the disc, and AO is the axis of rotation.

where τ_y is the yield stress, e_{ij} is the rate of deformation tensor, μ_p is the plastic dynamic viscosity, $\eta(\dot{\gamma})$ is the apparent viscosity, and $\dot{\gamma}$ ($\dot{\gamma} \equiv \sqrt{\frac{1}{2}\left|e_{ij}e_{ij}\right|}$) is the second invariant of the rate of deformation tensor. The physical significance of Equation (7) is that there is a threshold value of the applied stress, known as the yield stress τ_y, below which a Bingham fluid does not exhibit any deformation-rate. Above the yield stress τ_y, a Bingham fluid exhibits fluid-like behaviour such that the effective viscosity is a non-linear function of the rate of deformation tensor itself. For von Kármán's swirling flows, the rotation of the disc causes the establishment of the stress field in the fluid.

A. Non-dimensional variables

The results, given in this paper, are presented in terms of a few non-dimensional variables and parameters. Two important non-dimensional numbers for explaining the flow of Bingham fluid above a rotating disc are the Bingham number *Bn* and the Reynolds number *Re*, given by the following relations:

$$Bn \equiv \tau_y / \left(\Omega \mu_p\right), \tag{8}$$

$$Re \equiv \left(\Omega r^2\right) / \nu_p. \tag{9}$$

In Equation (9), ν_p denotes the plastic kinematic viscosity of a Bingham fluid. The Bingham number *Bn* represents the non-dimensional yield stress. The present theoretical study has been carried out for a range of *Bn* (from 0 to 50). The characteristics of laminar and turbulent flows, and, the

This article is copyrighted as indicated in the article. Reuse of AIP content is subject to the terms at: http://scitation.aip.org/termsconditions. Downloaded to IP: 203.110.246.23 On: Sun, 10 Jan 2016 14:27:14

transition from laminar to turbulent flow depend on the value of the Reynolds number Re. For a Newtonian fluid, the transition from laminar to turbulent flow occurs when Re is greater than 10^5.[33] We could not find in the literature a similar limiting value as the critical Re for a Bingham fluid. In the present paper, only laminar flow has been studied. The maximum Re used in the present study is kept below 10^5.

For a particular Ω and ν_p, Re increases with radius r. Therefore, the following relation shows that $\sqrt{Re}$, denoted as $\Re$, can be interpreted as a non-dimensional radius:

$$\Re = r/\sqrt{\nu_p/\Omega} = \sqrt{Re}. \tag{10}$$

The non-dimensional axial coordinate, ζ, is similarly defined by the relation

$$\zeta = z/\sqrt{\nu_p/\Omega}. \tag{11}$$

Three variables $\hat{V}_r$, $\hat{V}_\theta$, and $\hat{V}_z$ are used to denote the non-dimensional radial velocity, non-dimensional tangential velocity, and non-dimensional axial velocity, respectively. The non-dimensionalization for $\hat{V}_r$, $\hat{V}_\theta$, and $\hat{V}_z$ is performed as follows:

$$\hat{V}_r = V_r/(r\Omega),\ \hat{V}_\theta = V_\theta/(r\Omega),\ \text{and}\ \hat{V}_z = V_z/\sqrt{\nu_p\Omega}. \tag{12}$$

III. CFD SIMULATION

Figure 1(a) shows the relevant fluid flow domain which is three dimensional. However, considering the axi-symmetry of the flow field, the present computation has been performed in a two dimensional geometry with appropriate equations for axi-symmetric flow. The two dimensional domain (i.e., OABR) for the computational study is represented in Figure 1(b). RO is the surface of the disc. AB and BR represent fluid boundaries, respectively, at the top and at the edge of the disc. OA is a part of the axis about which the disc is rotating at an angular speed Ω. Steady state solutions are computed for fluids with various values of Bn.

A. Computational schemes

Equations (1)–(4) are solved by a commercially available CFD software Fluent 6.3.26. Two dimensional, steady, double-precision, pressure based, implicit solver is used. The velocity formulation is in the absolute frame of reference. Axi-symmetric swirl model[34] is utilized to calculate the tangential component of velocity V_θ. The SIMPLE algorithm, with second order upwind scheme for momentum and 'Standard' scheme (pressure on the control-faces are obtained through interpolation of their corresponding cell-centre pressure values) for discretizing the pressure equation, are utilized. Under-relaxation factors for momentum (radial and axial components), swirl (tangential component), pressure, density, and body force are chosen as 0.7, 0.9, 0.6, 1, and 1, respectively. The convergence criterion for the maximum "scaled" residual[34] is set as 10^{-7}.

Equation (5), which is a no slip boundary condition, can be implemented directly in a CFD simulation. Also, a non-zero rotational speed Ω is set on the disc-surface (which is at $z = 0$). However, Equation (6) cannot be implemented directly in a CFD simulation. A sufficiently large but finite value of z is used to represent $z \to \infty$. Pressure outlet boundary condition is used on the surface AB to represent the ambient condition where both V_r and V_θ asymptotically approach to zero. In the CFD, two additional boundary conditions are required. The first is an axis boundary condition which is set at AO of the computational domain OABR. The second is a pressure outlet boundary condition which is set at BR of the computational domain OABR.

B. Modeling a Bingham fluid in CFD simulation

It is difficult to implement the constitutive relation for a Bingham fluid, as given by Equation (7), in a CFD simulation. Moreover, one is restricted to the available options in the software.

This article is copyrighted as indicated in the article. Reuse of AIP content is subject to the terms at: http://scitation.aip.org/termsconditions. Downloaded to IP: 203.110.246.23 On: Sun, 10 Jan 2016 14:27:14

The constitutive relation proposed by O'Donovan and Tanner[35] is therefore used in the present computations. According to O'Donovan and Tanner, the stress tensor τ_{ij} of a Bingham fluid can be expressed as

$$\begin{aligned} \tau_{ij} &= \mu_y e_{ij}, \quad \text{for } |\dot{\gamma}| \le \tau_y/\mu_y \\ \tau_{ij} &= \tau_y + \mu_p \left(e_{ij} - \tau_y/\mu_y\right), \quad \text{for } |\dot{\gamma}| > \tau_y/\mu_y. \end{aligned} \tag{13}$$

Equation (13) represents a bi-viscosity model, where μ_p is the plastic dynamic viscosity and μ_y is the yielding viscosity. A bi-viscosity model is a viscosity regularisation method. Many advantages of a viscosity regularisation method are described in Ref. 36. However, in some cases, the prediction of a regularized Bingham model may differ from that of the ideal Bingham model. For example, Chatzimina *et al.*[37] have shown the difference between the predictions of the ideal and the regularized Bingham model in some particular situations of Couette and Poiseuille flows. Thus, a careful implementation of the bi-viscosity model is necessary to achieve an accurate CFD solution. Fluent 6.3.26 provides the Herschel–Bulkley fluid model[38] which can be transformed into Equation (13) by considering the power-law index of Herschel–Bulkley model to be unity. The ratio μ_y/μ_p needs to be set at a large value. O'Donovan and Tanner,[35] while solving a squeeze film problem, had observed that for implementing Bingham fluid model effectively in a numerical study, the yielding viscosity should be 1000 times the plastic viscosity. In their recent study, Turan *et al.*[32] used the model of O'Donovan and Tanner[35] for studying natural convection in a square enclosure. The value of μ_y/μ_p used by Turan *et al.*[32] is 10 000. The value of μ_y/μ_p is set at 50 000 for the present study. The rationale for this choice is examined in the Appendix.

C. Geometry of the computational domain and grid independence test

The geometry of the computational domain and the computational grid are generated by the commercially available software GAMBIT 2.4.6. All computations for the present study are carried out in a particular computational domain. Theory[2] shows that the non-dimensional boundary layer thickness ($\hat{\delta} \equiv \delta/\sqrt{\nu_p/\Omega}$) for von Kármán swirling flow of a Newtonian fluid is 5.5. The present computations show that $\hat{\delta}$ increases with *Bn*. Hence, the ζ value for the boundary AB of the computational domain should be sufficiently larger than 5.5. The maximum value of ζ is therefore taken as 22. Similarly, the computational domain is extended to a sufficiently large value of $\mathfrak{R}$ so that the Newtonian limits for various Bingham fluids can be captured (this can be understood after reading the discussion of Section V F). However, an arbitrarily large value of $\mathfrak{R}$ cannot also be taken if laminar flow is considered (Section II A). The computational resources and required computational time also increase with increasing $\mathfrak{R}$. As a balance between these opposite demands, the maximum value of $\mathfrak{R}$ is taken to be 270 in the present computations.

A grid independence test has been carried out (Table I showing a few pertinent details), and based on this study, a total 52 272 (363×144) mapped, quadrilateral computational cells are used for the results presented in this paper. The grids are distributed in the radial and axial directions in accordance with the difference in the flow physics in the two directions. The grid distribution in the axial direction is non-uniform with very small grid size close to the disc-surface (to capture the velocity gradient on the surface accurately) and with progressively larger grid size towards the boundary AB. In course of the present study, it has been found that, for a Bingham fluid, the flow field changes rapidly at small $\mathfrak{R}$ and slowly at large $\mathfrak{R}$ (discussed in Section V). In order to capture this effect properly, the grids in the radial direction are divided into two zones—non-uniform and uniform. From $\mathfrak{R} = 0$ to $\mathfrak{R} = 163$, non-uniform grids are used. Within this radial span, 300 grids are distributed with a successive ratio of 1.01. For $\mathfrak{R} > 163$, the grid distribution in the radial direction is uniform and the grid size is equal to the size of the last computational cell of the non-uniform zone.

All three non-dimensional velocity components ($\hat{V}_r$, $\hat{V}_\theta$, and $\hat{V}_z$) asymptotically attain a constant value for a sufficiently large value of ζ. At large ζ, both $\hat{V}_r$ and $\hat{V}_\theta$ become zero; $\hat{V}_z$, on the other hand, attains a constant negative value. This constant value for $\hat{V}_z$ at a large ζ is denoted as $\hat{V}_z(\infty)$. Among several output parameters of the CFD simulations, $\hat{V}_z(\infty)$ is selected as a testing parameter for the grid independence test. The values of $\hat{V}_z(\infty)$ for various grid distributions are reported in Table I.

This article is copyrighted as indicated in the article. Reuse of AIP content is subject to the terms at: http://scitation.aip.org/termsconditions. Downloaded to IP: 203.110.246.23 On: Sun, 10 Jan 2016 14:27:14

TABLE I. Grid independence test (CFD data given at $Re = 3000$).

Grid distribution	Number of grids in r and z directions	Total number of grids	$\hat{V}_z(\infty)$ for $Bn = 50$ from CFD	$\hat{V}_z(\infty)$ for $Bn = 0$ from CFD	$\hat{V}_z(\infty)$ for $Bn = 0$ from numerical solution[39]
Coarse	(180 × 72)	12 960	−0.6202	−0.8879	−0.8845
Standard	(363 × 144)	52 272	−0.6348	−0.8847	
Fine	(500 × 200)	100 000	−0.6373	−0.8847	

D. Validation

CFD solutions, in general, need to be validated with respect to any experimental or authentic theoretical results. Unfortunately, we could not find any reliable data in the literature for validating the results corresponding to the flow of a Bingham fluid above a rotating disc. On the other hand, for von Kármán's flow in a Newtonian fluid, many authentic studies are available in the literature. Among these available results, the numerical solution given by Owen and Rogers[39] is utilized for validating the present CFD solution in the limit $Bn \to 0$. Figure 2 shows the axial variation of non dimensional velocity components $\hat{V}_r$, $\hat{V}_\theta$, and $\hat{V}_z$ obtained from the present CFD simulations at $Bn \to 0$. It can be observed that present CFD solution at $Bn \to 0$ agrees well with the numerical solution given by Owen and Rogers.[39] This proves that the computational methodology, used for the present CFD simulations, is able to reproduce the classical solution of von Kármán swirling flow. The same computational methodology is also used for a Bingham fluid ($Bn > 0$). The only alternation required is in setting the properties of a Bingham fluid which are different from that of a Newtonian fluid.

IV. SIMPLIFIED SEMI-ANALYTICAL APPROACHES

In Section II, the governing equations [Equation (1)–(4)] for the flow of a Bingham fluid above a rotating disc are provided. A procedure to solve Equations (1)–(4) by using CFD is described in

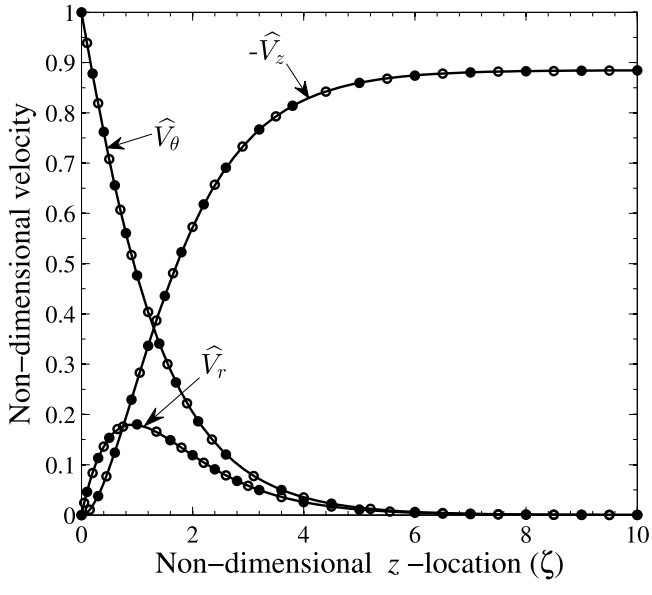

FIG. 2. Non-dimensional velocity profiles for the steady flow of a Newtonian fluid ($Bn = 0$) above a rotating disc (von Kármán's swirling flow). [(——) Results obtained from the present CFD simulation at $Bn = 0$; (○) numerical solution of Equations (17)–(19) as $Bn \to 0$; (●) numerical solution of Owen and Rogers.[39]]

This article is copyrighted as indicated in the article. Reuse of AIP content is subject to the terms at: http://scitation.aip.org/termsconditions. Downloaded to IP: 203.110.246.23 On: Sun, 10 Jan 2016 14:27:14

Section III. In this section, a simplified semi-analytical approach is presented. Additional assumptions regarding the fluid flow field are needed for the semi-analytical approach. These assumptions are made by taking cue from von Kármán solution for a Newtonian fluid. It is assumed that, at a particular radius r, separation of variables can be applied to express both radial velocity V_r and tangential velocity V_θ (i.e., both V_r and V_θ can be expressed as a product of a radial function and an axial function). Furthermore, at a particular radius r, the radial function describing V_θ is directly proportional to r. The axial velocity V_z, at a particular radius r, is assumed to be a function only of z. The variation of radial, tangential, and axial velocities can be mathematically expressed as follows:

$$\begin{aligned} V_r &= r\Omega\, e^{-yn}\, F(\zeta), \\ V_\theta &= r\Omega\, G(\zeta), \\ V_z &= \sqrt{\nu_p \Omega}\, H(\zeta), \end{aligned} \tag{14}$$

where

$$yn = \frac{Bn}{Re^m} = cm^n. \tag{15}$$

In Equation (15), the variable yn is introduced as a corrective yield number, the parameter m is a function of Bn and Re (i.e., of radius r), and the parameters c and n are considered to be constant. For this work, the most suitable values of c and n are determined by comparing the predictions of the semi-analytical formulation with numerous CFD simulations at various Bn. On the basis of such extensive comparison, the following values are recommended: $c = 7.27$ and $n = 5$. In Equation (14), the expressions of V_θ and V_z are the same as given by von Kármán.[1] However, the radial function in the expression of V_r (i.e., $r\Omega\, e^{-yn}$) is different from the radial function considered by von Kármán (i.e., $r\Omega$). For a Newtonian fluid ($Bn = 0$), Equation (15) shows that e^{-yn} is equal to one. Hence, for a Newtonian fluid, Equation (14) totally corresponds to von Kármán's transformation that is $V_r = r\Omega\, F(\zeta)$, $V_\theta = r\Omega\, G(\zeta)$, and $V_z = \sqrt{\nu_p \Omega}\, H(\zeta)$. Unlike von Kármán's solution method, however, the radial variations of the functions F, G, and H for a Bingham fluid ($Bn > 0$) are to be determined, as described below.

The following relations for the non-dimensional velocity components $\hat{V}_r$, $\hat{V}_\theta$, and $\hat{V}_z$ can be derived by using Equations (12) and (14),

$$\begin{aligned} \hat{V}_r &= e^{-yn}\, F, \\ \hat{V}_\theta &= G, \\ \hat{V}_z &= H. \end{aligned} \tag{16}$$

It is possible to transform partial differential equations (1)–(4) into ordinary differential equations by applying Equation (14). Considering the fluid to be inelastic, the term $(\tau_{rr} - \tau_{\theta\theta})/r$ in Equation (2) is neglected. Using Equation (16), these ordinary differential equations can be expressed in the following form:

$$2\hat{V}_r(1 + m\, yn\, \Lambda) + \hat{V}_z' = 0, \tag{17}$$

$$\begin{aligned} &(1 + 2m\, yn\, \Lambda)\, \hat{V}_r^2 - \hat{V}_\theta^2 + \hat{V}_z \hat{V}_r' = \\ &(1 + Bn/\hat{\gamma})\hat{V}_r'' - \frac{Bn\, \hat{V}_r'}{2\hat{\gamma}^3}\chi_1 + \frac{2}{Re}(1 + Bn/\hat{\gamma})\hat{V}_r\chi_2 - \frac{Bn}{Re\hat{\gamma}^3}(1 + 2m\, yn\, \Lambda)\hat{V}_r\chi_3, \end{aligned} \tag{18}$$

$$2\hat{V}_r\hat{V}_\theta + \hat{V}_z\hat{V}_\theta' = (1 + Bn/\hat{\gamma})\hat{V}_\theta'' - \frac{Bn\, \hat{V}_\theta'}{2\hat{\gamma}^3}\chi_1. \tag{19}$$

In Equations (17)–(19), the superscripts, single prime and double prime, denote $\partial/\partial\zeta$ and $\partial^2/\partial\zeta^2$, respectively. Λ, $\hat{\gamma}$ (non-dimensional second invariant of the rate of deformation tensor), χ_1, χ_2, and χ_3 are as follows:

$$\Lambda = \frac{n}{n + m \log_e Re}, \tag{20}$$

This article is copyrighted as indicated in the article. Reuse of AIP content is subject to the terms at: http://scitation.aip.org/termsconditions. Downloaded to IP: 203.110.246.23 On: Sun, 10 Jan 2016 14:27:14

$$\hat{\dot{\gamma}} = \dot{\gamma}/\Omega = \sqrt{2\hat{V}_r^2\left\{1 + (1 + 2m\, yn\, \Lambda)^2\right\} + 2(\hat{V}_z')^2 + Re\left\{(\hat{V}_r')^2 + (\hat{V}_\theta')^2\right\}}, \tag{21}$$

$$\chi_1 = 4\hat{V}_r\hat{V}_r'\left\{1 + (1 + 2m\, yn\, \Lambda)^2\right\} + 4\hat{V}_z'\,\hat{V}_z'' + 2Re\left\{\hat{V}_r'\hat{V}_r'' + \hat{V}_\theta'\hat{V}_\theta''\right\}, \tag{22}$$

$$\chi_2 = 2m\, yn\, \Lambda + 4m^2 yn^2\, \Lambda^2 - 4m^2 yn\, \Lambda^2 + 2m\, yn\, \Lambda^* + 2m^*\, yn\, \Lambda, \tag{23}$$

$$\begin{aligned}\chi_3 = {} & 8\hat{V}_r^2(1 + 2m\, yn\, \Lambda)(m^*\, yn\, \Lambda + m\, yn\, \Lambda^* - 2m^2\, yn\, \Lambda^2) + \\ & 8m\, yn\, \Lambda\, \hat{V}_r^2\left\{1 + (1 + 2m\, yn\, \Lambda)^2\right\} + 2Re\left\{(\hat{V}_r')^2 + (\hat{V}_\theta')^2\right\} + 4m\, yn\, \Lambda\, Re(\hat{V}_r')^2.\end{aligned} \tag{24}$$

The expressions for m^* and Λ^* used in Equations (23) and (24) are given as

$$m^* = r\frac{dm}{dr} = -\frac{2m^2}{(n + m\log_e Re)}, \tag{25}$$

$$\Lambda^* = r\frac{d\Lambda}{dr} = -\frac{n}{(n + m\log_e Re)^2}\left(m^*\log_e Re\ + 2m\right). \tag{26}$$

The ordinary differential equations for a Bingham fluid given above are based on Equation (14). For $Bn > 0$, Equation (14) is different from von Kármán's transformation. It will be interesting to investigate what happens if one does not apply the factor $\exp(-yn)$ in Equation (14). The non dimensional velocity components can then be expressed as follows:

$$\begin{aligned}\hat{V}_r &= F(\zeta),\\ \hat{V}_\theta &= G(\zeta),\\ \hat{V}_z &= H(\zeta).\end{aligned} \tag{27}$$

It is to be realized that although Equation (27) used in this limiting theory for a Bingham fluid appears to be the same as that used by von Kármán for a Newtonian fluid, there is, however, an important underlying difference. In von Kármán's solution, the functions F, G, and H have the same values at all $\Re$. This is not true in the present case. The radial variations of the functions F, G, and H are to be determined for a Bingham fluid as described below. To remind ourselves of this difference, we would refer to Equation (27) as the modified von Kármán's transformation in the rest of the paper.

Using modified von Kármán's transformation into the partial differential equations (1)–(4) and considering the fluid to be inelastic, the following set of ordinary differential equations is obtained:

$$2\hat{V}_r + \hat{V}_z' = 0, \tag{28}$$

$$\begin{aligned}\hat{V}_r^2 - \hat{V}_\theta^2 + \hat{V}_z\hat{V}_r' = {} & \left(1 + \frac{Bn}{\hat{\dot{\gamma}}}\right)\hat{V}_r'' - \frac{2Bn}{\hat{\dot{\gamma}}^3}\hat{V}_r\left\{(\hat{V}_r')^2 + (\hat{V}_\theta')^2\right\} \\ & - \frac{Bn}{2\hat{\dot{\gamma}}^3}\hat{V}_r'\left[8\hat{V}_r\hat{V}_r' + 4\hat{V}_z'\,\hat{V}_z'' + 2Re\left\{\hat{V}_r'\,\hat{V}_r'' + \hat{V}_\theta'\hat{V}_\theta''\right\}\right],\end{aligned} \tag{29}$$

$$2\hat{V}_r\hat{V}_\theta + \hat{V}_z\hat{V}_\theta' = \left(1 + \frac{Bn}{\hat{\dot{\gamma}}}\right)\hat{V}_\theta'' - \frac{Bn}{2\hat{\dot{\gamma}}^3}\hat{V}_\theta'\left[8\hat{V}_r\hat{V}_r' + 4\hat{V}_z'\,\hat{V}_z'' + 2Re\left\{\hat{V}_r'\hat{V}_r'' + \hat{V}_\theta'\hat{V}_\theta''\right\}\right]. \tag{30}$$

The non-dimensional second invariant of the rate of deformation $\hat{\dot{\gamma}}$ used in Equations (29) and (30) can be expressed as follows:

$$\hat{\dot{\gamma}} = \dot{\gamma}/\Omega = \sqrt{4\hat{V}_r^2 + 2(\hat{V}_z')^2 + Re\left\{(\hat{V}_r')^2 + (\hat{V}_\theta')^2\right\}}. \tag{31}$$

Equations (28)–(30), which are obtained here as a limiting case ($yn \to 0$) of our original formulation [Equations (17)–(19)], are similar to those of Ahmadpour and Sadeghy;[29] their solutions however contain several errors (one example being that the quantitative values given in their paper for the ζ-variation of the radial velocity at all non-zero Bingham numbers are erroneous; some of their equations also contain errors). The two sets of ODEs, Equations (17)–(19) and (28)–(30), are solved numerically for particular values of Re and Bn by using the boundary conditions as follows:

$$\text{at } \zeta = 0,\ \hat{V}_r = 0,\ \hat{V}_\theta = 1, \text{ and } \hat{V}_z = 0, \tag{32}$$

This article is copyrighted as indicated in the article. Reuse of AIP content is subject to the terms at: http://scitation.aip.org/termsconditions. Downloaded to IP: 203.110.246.23 On: Sun, 10 Jan 2016 14:27:14

$$\text{as } \zeta \to \infty,\ \hat{V}_r \to 0, \text{ and } \hat{V}_\theta \to 0. \tag{33}$$

The following procedure is adopted for solving Equations (17)–(19) and (28)–(30). At first, they are converted into a set of five first order ordinary differential equations involving $\hat{V}_r$, $\hat{V}_\theta$, $\hat{V}_z$, $\hat{V}_r'$, $\hat{V}_\theta'$, and $\hat{V}_z'$. These five equations are then solved by the shooting method. In this numerical technique, the values of $\hat{V}_r'$ and $\hat{V}_\theta'$ at $\zeta = 0$ are initially guessed. Then, the five first-order ODEs are integrated numerically by fourth order Runge-Kutta method. The integrated values of $\hat{V}_r$ and $\hat{V}_\theta$ at $\zeta \to \infty$ are not in general equal to the actual boundary values as given in Equation (33). Newton's method for simultaneous non-linear equations[40] is utilized for finding the roots of the boundary residuals in order to obtain the next guess for $\hat{V}_r'(0)$ and $\hat{V}_\theta'(0)$. This iterative procedure is repeated until the residuals become less than a very small value (a relative error of 10^{-8} is used as the convergence criterion for the present work).

Present numerical solution of Equations (17)–(19) for $Bn = 0$ is validated with the numerical solution given in Ref. 39 for a Newtonian fluid. According to the solution given in Ref. 39, the values of $\hat{V}_r'(0)$, $\hat{V}_\theta'(0)$, and $\hat{V}_z(\infty)$ are 0.5102, −0.6159, and −0.8845, respectively. The values of $\hat{V}_r'(0)$, $\hat{V}_\theta'(0)$, and $\hat{V}_z(\infty)$, which are obtained from the present numerical solution, are 0.5102, −0.6159, and −0.8845, respectively. Figure 2 shows that the ζ-variations of $\hat{V}_r$, $\hat{V}_\theta$, and $\hat{V}_z$ obtained from the present numerical solution of Equations (17)–(19) for $Bn = 0$ agree well with the ζ-variations of $\hat{V}_r$, $\hat{V}_\theta$, and $\hat{V}_z$ given by Owen and Rogers.[39] In Sec. V, solutions of Equations (17)–(19) have been compared with full CFD simulations for various values of Bn.

V. RESULTS AND DISCUSSION

Results from CFD simulations and semi-analytical approaches are presented and critically analysed here. In order to streamline the physical understanding, the analysis is grouped in seven sub-sections.

A. Velocity distributions

In the present work, the non-dimensional velocity components ($\hat{V}_\theta$, $\hat{V}_r$, and $\hat{V}_z$) in the axi-symmetric flow domain are calculated by three complementary but separate ways: (i) full CFD simulations and (ii) semi-analytical approach involving Equations (17)–(19), and (iii) semi-analytical approach involving Equations (28)–(30).

Figures 3–5 show the axial (i.e., ζ) distributions of $\hat{V}_\theta$, $\hat{V}_r$, and $\hat{V}_z$, respectively. This study is conducted at a moderate value of non-dimensional radius $\Re$ which corresponds to $Re = 3000$ (Equation (10) shows that $\Re = r/\sqrt{\nu_p/\Omega} = \sqrt{Re}$). The representative calculations displayed in Figures 3–5 are carried out for three different values of Bn (10, 30, and 50).

It can be observed from Figure 3 that, at all values of Bn, the ζ-distribution of $\hat{V}_\theta$ obtained by Equations (17)–(19) agree well with that obtained by CFD simulations. The value of $\hat{V}_\theta$ is greatest at the disc surface where it is equal to one. $\hat{V}_\theta$ decreases with increasing ζ, asymptotically approaching zero at sufficiently large ζ. When Bn increases, two major changes in the $\hat{V}_\theta$-profile can be observed. First of all, the value of $\hat{V}_\theta$ increases at all nonzero ζ. Second, with an increase in ζ, the rate of decrease of $\hat{V}_\theta$ decreases. The physical implication of these two effects is that, with an increase in the Bingham number, the rotation imparted by the solid disc penetrates further up into the fluid. Why $\hat{V}_\theta$ (at a particular non-zero value of ζ) increases with an increase in Bn can be explained in the following way. Consider a limiting case when Bn is very large ($Bn \to \infty$). Then, the rotation of the fluid at the steady state (for finite $\Re$) will be comparable to a solid-body rotation, thus acquiring the angular speed of the disc, Ω. The high effective viscosity at large Bn inhibits the decay of tangential velocity in the axial direction. Hence, when Bn increases, the decay of tangential velocity in the axial direction decreases.

The fluid above the rotating disc is pumped radially outward. The radial flow is a kind of secondary flow which is generated because of the centripetal acceleration. Figure 4 shows the axial variation of the non-dimensional radial velocity $\hat{V}_r$ for a Bingham fluid. It can be seen that the

This article is copyrighted as indicated in the article. Reuse of AIP content is subject to the terms at: http://scitation.aip.org/termsconditions. Downloaded to IP: 203.110.246.23 On: Sun, 10 Jan 2016 14:27:14

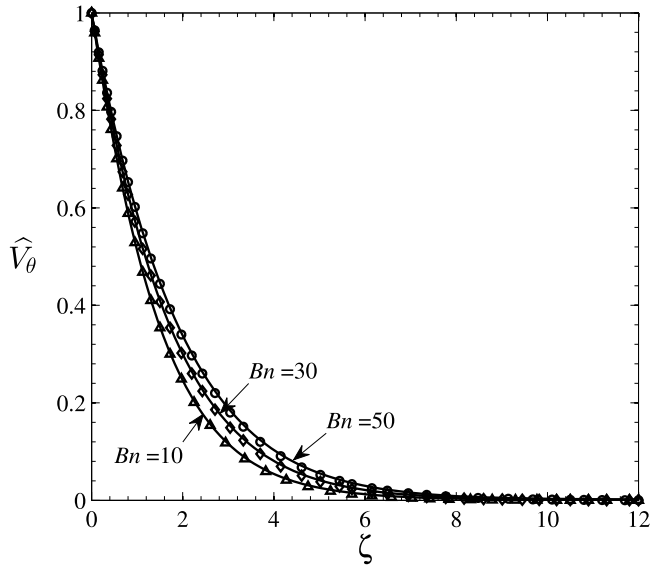

FIG. 3. Non-dimensional tangential velocity ($\hat{V}_\theta$) profiles for a Bingham fluid at various values of *Bn*. [(——) Present CFD simulations for various *Bn*; prediction of Equations (17)–(19): (△) *Bn* = 10, (◊) *Bn* = 30, (○) *Bn* = 50. All profiles correspond to *Re* = 3000.]

$\hat{V}_r$ obtained by Equations (17)–(19) agrees well with the $\hat{V}_r$ obtained by CFD simulation. At the disc-surface, the value of $\hat{V}_r$ is zero due to the no slip boundary condition. With an increase in ζ, $\hat{V}_r$ attains a maxima near the disc surface and then decreases, and ultimately becomes zero. When *Bn* increases, three major changes in the $\hat{V}_r$-profiles can be observed. First of all, the maximum value of $\hat{V}_r$ decreases. Secondly, the corresponding ζ, at which this maxima occurs, increases. Thirdly, after attaining the maxima, the rate of decrease of $\hat{V}_r$ with an increase in ζ decreases. As a consequence, $\hat{V}_r$-profiles corresponding to any two different *Bn* cross each other; this means that $\hat{V}_r$ is smaller for greater *Bn* in the region between the origin and the cross-over point whereas $\hat{V}_r$ is greater for higher *Bn* when ζ is larger than the coordinate of the cross-over point. The underlying physics for this crossing over of $\hat{V}_r$-profiles is as follows. There are two opposing forces acting on the fluid above

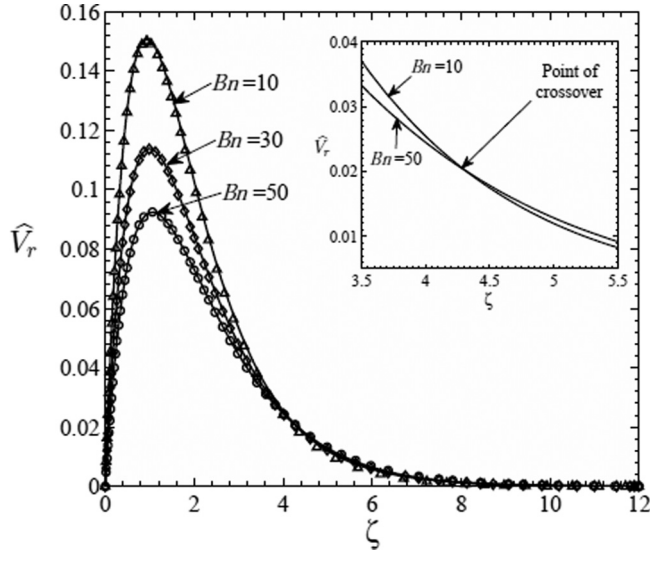

FIG. 4. Non-dimensional radial velocity ($\hat{V}_r$) profiles for a Bingham fluid at various values of *Bn*. [(——) Present CFD simulations for various *Bn*; prediction of Equations (17)–(19): (△) *Bn* = 10, (◊) *Bn* = 30, (○) *Bn* = 50. All profiles correspond to *Re* = 3000.]

This article is copyrighted as indicated in the article. Reuse of AIP content is subject to the terms at: http://scitation.aip.org/termsconditions. Downloaded to IP: 203.110.246.23 On: Sun, 10 Jan 2016 14:27:14

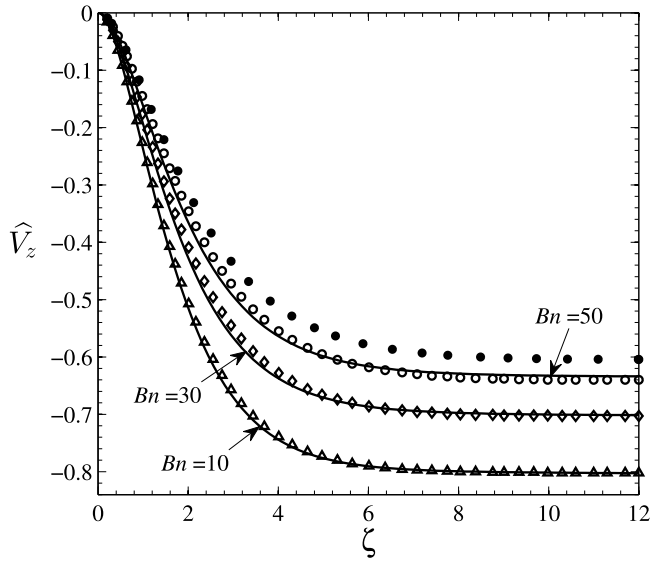

FIG. 5. Non-dimensional axial velocity ($\hat{V}_z$) profiles for a Bingham fluid at various values of *Bn*. [(——) Present CFD simulations for various *Bn*; prediction of Equations (17)–(19): (△) $Bn = 10$, (◊) $Bn = 30$, (○) $Bn = 50$; (●) prediction of Equations (28)–(30) for $Bn = 50$. All profiles correspond to $Re = 3000$.]

the rotating disc in the radial direction. These two are viscous force and inertial force. Near the disc-surface, the effect of the viscous force dominates over the inertial force. The effect of viscous force in radial direction is such that it opposes the radial outflow of fluid (at disc-surface, the radial velocity is zero). With an increase in *Bn*, viscous force increases. Hence, near the disc, $\hat{V}_r$ decreases with an increase in *Bn*. When ζ increases, inertial force gradually overtakes the effect of viscous force. It has already been shown that at any particular *Re*, the non-dimensional tangential velocity $\hat{V}_\theta$ increases with an increase in *Bn*. The inertial force increases with an increase in tangential velocity. Therefore, when ζ is larger than the coordinate of the cross-over point, $\hat{V}_r$ increases with an increase in *Bn*.

The axial flow (towards the disc) occurs to supply the fluid within the boundary layer which will otherwise be evacuated for continuous radial-outflow. Figure 5 shows the axial variation for the non-dimensional axial velocity $\hat{V}_z$ of a Bingham fluid. It can be observed that the $\hat{V}_z$ obtained by Equations (17)–(19) are in close agreement with the $\hat{V}_z$ obtained by CFD simulations. The same figure also contains the solutions obtained by Equations (28)–(30) at $Bn = 50$ (results for only one Bingham number are included so that the clarity of the figure is not jeopardized). A significant discrepancy can be observed between the prediction of equations of (28)-(30) and the prediction of CFD, thus establishing the superiority of Equations (17)–(19) over Equations (28)–(30). Figure 5 shows that the axial velocity is negative in the flow domain. It is so because the ambient fluid flows towards the disc. The magnitude of $\hat{V}_z$ decreases towards the disc and becomes zero at the disc surface because of the no penetration boundary condition. With an increase in *Bn*, the magnitude of $\hat{V}_z$ at any particular ζ decreases (so long as $\mathfrak{R}$ is not too large). It is so because the net radial outflow [across a line connecting the points $(\mathfrak{R}, 0)$ and $(\mathfrak{R}, \zeta)$] decreases with an increase in *Bn*.

Figure 6 shows the variation of three normalized velocity components ($\tilde{V}_\theta$, $\tilde{V}_r$, and $\tilde{V}_z$) with non-dimensional radius $\mathfrak{R}$ for $Bn = 50$. All variables are calculated by three methods: CFD simulations, predictions of Equations (17)–(19), and, predictions of Equations (28)–(30). Each component of velocity is normalized by its respective value at $\mathfrak{R} = 160$ determined by CFD. Figures 6(a)–6(c) display, respectively, the tangential ($\tilde{V}_\theta$), radial ($\tilde{V}_r$), and axial ($\tilde{V}_z$) components, all calculated at a particular ζ ($\zeta = 5$).

It can be observed from Figures 6(a)–6(c) that the numerical solution of Equations (17)–(19) captures the $\mathfrak{R}$-variation of all three velocity components and matches well with the full CFD simulations, including the complex variation at small $\mathfrak{R}$. Figures 6(a)–6(c) also demonstrate that

This article is copyrighted as indicated in the article. Reuse of AIP content is subject to the terms at: http://scitation.aip.org/termsconditions. Downloaded to IP: 203.110.246.23 On: Sun, 10 Jan 2016 14:27:14

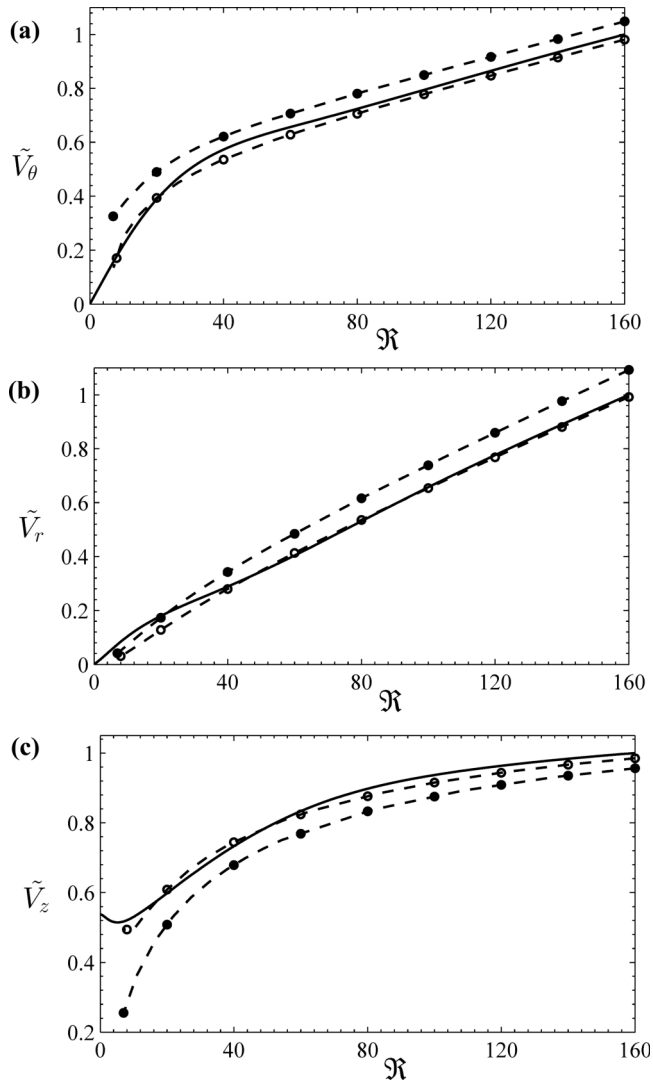

FIG. 6. Comparisons of radial-variation for three normalized velocity components at a particular $\zeta(\zeta = 5)$ obtained by three different solution methods. (a) Normalized tangential velocity $\tilde{V}_\theta$, (b) normalized radial velocity $\tilde{V}_r$, (c) normalized axial velocity $\tilde{V}_z$. [Keys for the three methods of calculation: (——) Present CFD simulations; (– –○– –) prediction of Equations (17)–(19); (– –●– –) prediction of Equations (28)–(30). All calculations correspond to $Bn = 50$. V_θ, V_r, and V_z (obtained from the three methods at any $\Re$) are normalized, respectively, with V_θ, V_r, and V_z obtained by CFD at $\Re = 160$.]

Equations (17)–(19) based on the transformation that is proposed here perform a lot better than Equations (28)–(30) based on modified von Kármán's similarity transformation. It may be remembered that Figure 5 also showed the superiority of the present formulation in predicting the ζ-variation of the velocity components. A subtle but striking feature of Figure 6 is that, although the correction factor $\exp(-yn)$ is applied only to the radial velocity component $\tilde{V}_r$ (see Equation (14)), the prediction of all three velocity components ($\tilde{V}_r$, $\tilde{V}_\theta$, and $\tilde{V}_z$) by the semi-analytical approach improves significantly. The magnitude of the correction factor $\exp(-yn)$ is plotted in Figure 7. With recommended values $c = 7.27$ and $n = 5$, Equation (15) completely prescribes the variation of yn as a function of Bn and Re.

B. A closed-form expression for the disc-torque

A constant torque has to be applied on the disc to maintain a steady rotational speed of the disc. The applied torque balances the resisting torque due to the viscous shear stress acting on

This article is copyrighted as indicated in the article. Reuse of AIP content is subject to the terms at: http://scitation.aip.org/termsconditions. Downloaded to IP: 203.110.246.23 On: Sun, 10 Jan 2016 14:27:14

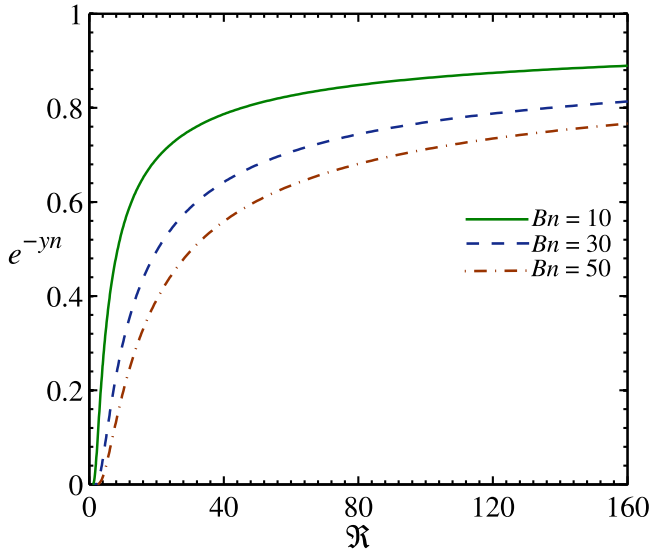

FIG. 7. Variation of the correction factor $\exp(-yn)$ with non-dimensional radius $\Re$ at various values of Bn.

the disc. Here, the torque is computed only on one side of the disc, the two sides being fluid dynamically symmetrical. Consider a segment from the disc-centre up to a radius r. The torque Γ_r required to maintain a steady rotational speed of this disc-segment can be determined by integrating $-2\pi r^2[\tau_{z\theta}]_{z=0}\,dr$ as follows:

$$\Gamma_r = -\int_0^r 2\pi r^2[\tau_{z\theta}]_{z=0}\,dr. \tag{34}$$

A non-dimensional moment coefficient $C_{m,\,r}$ can be defined for the disc-segment of radius r as follows:

$$C_{m,\,r} = \Gamma_r/\left(0.5\rho\Omega^2 r^5\right). \tag{35}$$

According to the semi-analytical approach described in Section IV, $[\tau_{z\theta}]_{z=0}$ can be written as

$$[\tau_{z\theta}]_{z=0} = \sqrt{\rho\Omega^3\mu_p}\left(1 + Bn/\left[\hat{\dot{\gamma}}\right]_{z=0}\right)\left[\hat{V}_\theta'\right]_{z=0} r. \tag{36}$$

By Equation (21), $\left[\hat{\dot{\gamma}}\right]_{z=0}$ can be expressed as

$$\left[\hat{\dot{\gamma}}\right]_{z=0} = \left[\sqrt{Re\left\{(\hat{V}_r')^2 + (\hat{V}_\theta')^2\right\}}\right]_{z=0}. \tag{37}$$

The superscript single prime denotes $\partial/\partial\zeta$ of the variable. It would be a formidable mathematical task to derive a closed-form expression for $C_{m,\,r}$ simply by substituting various expressions of Equations (34), (36), and (37) into Equation (35). Therefore, a few approximations are made here, the validity of which has been assessed below by comparing the prediction of the so-derived closed-form analytical expression for $C_{m,\,r}$ and that from the full CFD simulation for $C_{m,\,r}$. The radial variation in $\left[\hat{V}_\theta'\right]_{z=0}$ and $\left[\hat{V}_r'\right]_{z=0}$ is neglected; their values at the disc periphery are assumed to apply over the whole disc surface. For simplification of notation, these peripheral values are denoted by $\hat{V}_\theta'(0)$ and $\hat{V}_r'(0)$ in the following discussion (i.e., $\hat{V}_\theta'(r = \sqrt{Re\nu_p/\Omega},\, z = 0)$ is denoted simply by $\hat{V}_\theta'(0)$ and $\hat{V}_r'(r = \sqrt{Re\nu_p/\Omega},\, z = 0)$ is denoted by $\hat{V}_r'(0)$). One can then integrate Equation (34) by substituting Equations (36) and (37) into it. Then, by substituting the integrated expression of Γ_r into Equation (35), the expression for $C_{m,\,r}$ can be finally shown to be

This article is copyrighted as indicated in the article. Reuse of AIP content is subject to the terms at: http://scitation.aip.org/termsconditions. Downloaded to IP: 203.110.246.23 On: Sun, 10 Jan 2016 14:27:14

$$C_{m,\,r} = -4\pi\,\hat{V}_\theta'(0)\left[\frac{Bn}{3\sqrt{Re\,\{\hat{V}_r'^2(0)+\hat{V}_\theta'^2(0)\}}}+\frac{1}{4}\right]\frac{1}{\sqrt{Re}}. \tag{38}$$

For particular values of Bn and Re, Equation (38) gives $C_{m,\,r}$ when the values of $\hat{V}_\theta'(0)$ and $\hat{V}_r'(0)$ are known. The values of $\hat{V}_\theta'(0)$ and $\hat{V}_r'(0)$ are obtained by solving Equations (17)–(19), but the advantage of using Equation (38) is that $\hat{V}_\theta'(0)$ and $\hat{V}_r'(0)$ need to be determined only at one particular value of the radius that corresponds to the Reynolds number in question.

Equation (38) produces the correct result for a Newtonian fluid in the limit $Bn \to 0$. From Equation (38), $\lim_{Bn\to 0} C_{m,r} = -\pi\,\hat{V}_\theta'(0)/\sqrt{Re}$ which is the same result as given by Childs.[2]

The validity of the approximations involved in the derivation of Equation (38) is assessed by comparing its predictions with the values of $C_{m,\,r}$ obtained by full CFD simulation which is free of the approximations. Table II shows such a comparison for various Bn at $Re = 200$, $Re = 3000$, and $Re = 20\,000$. It can be seen that Equation (38) predicts the values of $C_{m,\,r}$ with high degree of accuracy over a large range of Bn and Re.

Equation (38) shows that, for a particular value of Re, the value of $C_{m,\,r}$ increases with an increase in Bn. $C_{m,\,r}$ for a Bingham fluid ($Bn > 0$) depends on both $\hat{V}_\theta'(0)$ and $\hat{V}_r'(0)$, whereas $C_{m,\,r}$ for a Newtonian fluid is independent of $\hat{V}_r'(0)$.

Equation (38) is new and has not appeared in the literature previously. The success of this equation is demonstrated in Table II. However, the mathematical derivation of Equation (38) neglects the radial variation in $\hat{V}_\theta'(0)$ and $\hat{V}_r'(0)$, so that analytical integration is possible. The success of Equation (38) in predicting the torque, however, does not allow one to conclude that von Kármán's original similarity transformation is adequate in describing the entire velocity field in a Bingham fluid. To shed further light, we have plotted the radial variation of the ζ-derivatives of the velocity components, i.e., $\hat{V}_\theta'$ and $\hat{V}_r'$, at three values of ζ in Figure 8. It is found that the derivatives $\hat{V}_\theta'$ and $\hat{V}_r'$ vary with the radial position in a complex fashion. $\hat{V}_\theta'$ is negative everywhere inside the boundary layer, since the tangential speed is maximum on the disc surface. $|\hat{V}_\theta'|$ on the surface is maximum for a Newtonian fluid. For a Bingham fluid, $|\hat{V}_\theta'|$ on the surface approaches the Newtonian limit

TABLE II. Non-dimensional moment coefficient ($C_{m,\,r}$) for various Bn at three different Re.

Re	Bn	$C_{m,\,r}$ from Equation (38)	$C_{m,\,r}$ from CFD simulations
200	0	0.137	0.136
	10	0.306	0.306
	20	0.499	0.499
	30	0.700	0.699
	40	0.903	0.900
	50	1.109	1.104
3000	0	0.035	0.035
	10	0.045	0.045
	20	0.056	0.056
	30	0.068	0.068
	40	0.081	0.081
	50	0.093	0.093
20 000	0	0.014	0.014
	10	0.015	0.015
	20	0.017	0.017
	30	0.018	0.018
	40	0.020	0.020
	50	0.022	0.022

This article is copyrighted as indicated in the article. Reuse of AIP content is subject to the terms at: http://scitation.aip.org/termsconditions. Downloaded to IP: 203.110.246.23 On: Sun, 10 Jan 2016 14:27:14

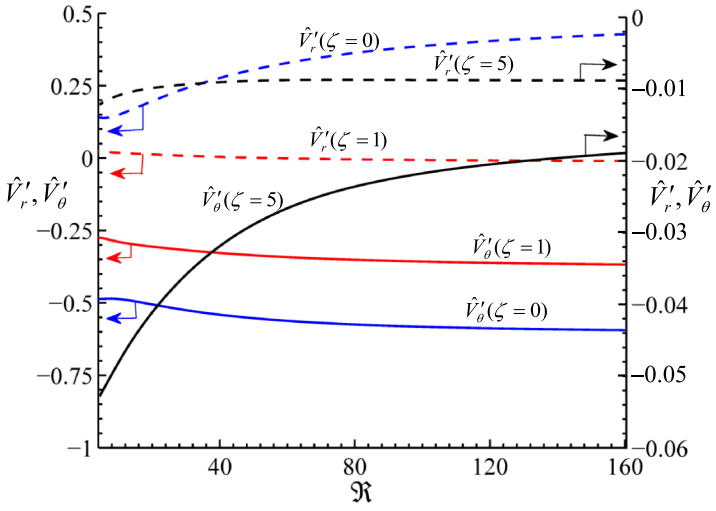

FIG. 8. Variations of $\hat{V}_\theta'$ and $\hat{V}_r'$ with non-dimensional radius $\mathfrak{R}$ at three values of ζ. [$\hat{V}_\theta' \equiv \partial/\partial\zeta(\hat{V}_\theta)$, $\hat{V}_r' \equiv \partial/\partial\zeta(\hat{V}_r)$. All calculations are performed at $Bn = 30$.]

(−0.6159) as the radius increases. The ζ profile of the radial velocity passes through a maxima. Therefore, $\hat{V}_r'$ is positive on the disc surface but becomes negative when the ζ-coordinate is above the point of maxima. $\hat{V}_r'$ on the disc surface is maximum for a Newtonian fluid. For a Bingham fluid, $\hat{V}_r'$ on the surface approaches the Newtonian limit (0.5102) as the radius increases.

There are two reasons for why Equation (38) works so well in practice. The first reason is that the radial variation of the ratio $\hat{V}_\theta'(0)/[\hat{V}_r'^2(0) + \hat{V}_\theta'^2(0)]$ is modest. The second reason is that, in the analytical integration process, the torque contribution of an elemental circular strip is weighted by r^3 (see Equations (34) and (36)), hence the torque contribution from the peripheral region of the disc (over which the variation in the ratio $\hat{V}_\theta'(0)/[\hat{V}_r'^2(0) + \hat{V}_\theta'^2(0)]$ is even smaller) dominates.

C. Volume flow rate

The net volume flow rate, which is pumped by the radial outflow, is entrained into the boundary layer by the axial flow. Hence, on one side of a disc, the net volume flow rate can be expressed as

$$\dot{Q}_r = 2\pi r \int_0^\infty V_r dz = -2\pi \int_0^r r[V_z]_{z\to\infty} dr, \tag{39}$$

where $\dot{Q}_r$ is the net volume flow rate through the curved surface of an infinitely long cylinder of radius r.

The non-dimensional volume flow rate is defined as

$$\hat{Q}_r = \dot{Q}_r / \left(\sqrt{\nu_p \Omega}\, \pi\, r^2\right). \tag{40}$$

For a Newtonian fluid, $[V_z]_{z\to\infty}$ in Equation (39) is independent of the local radius r. Thus, the integration can be performed analytically and results into the simple expression $\hat{Q}_r = -[1/\sqrt{\nu_p\Omega}][V_z]_{z\to\infty}$ as given by Childs.[2] However, for a Bingham fluid, it is difficult to evaluate the integration analytically because $[V_z]_{z\to\infty}$ varies with r and a closed-form expression for this variation is not available. (The integration is erroneously evaluated in Ref. 29 by taking $[V_z]_{z\to\infty}$ outside of the integral. Thus, the expression of $\hat{Q}_r$ and the values of $\hat{Q}_r$ given in Ref. 29 are inappropriate.) The integration is performed here numerically with the data obtained from CFD simulations. Figure 9 shows the variation of $\hat{Q}_r$ with Bn at three values of non-dimensional radius $\mathfrak{R}$. At a fixed value of $\mathfrak{R}$, $\hat{Q}_r$ decreases with an increase in Bn. For $Bn = 0$, the non-dimensional volume flow rate attains the Newtonian limit (0.8845) at any radius.

This article is copyrighted as indicated in the article. Reuse of AIP content is subject to the terms at: http://scitation.aip.org/termsconditions. Downloaded to IP: 203.110.246.23 On: Sun, 10 Jan 2016 14:27:14

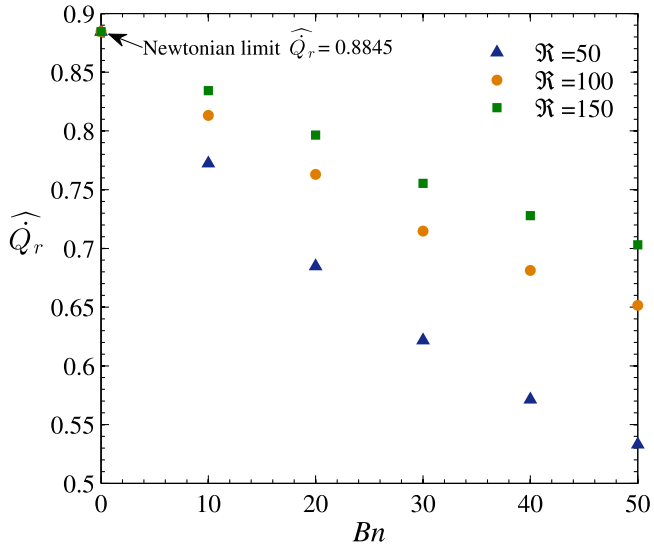

FIG. 9. Variation in non-dimensional volume flow rate with Bingham number.

D. Streamlines

The steady state velocity fields in the axi-symmetric flow domain above a rotating disc are calculated by CFD simulations. Once the velocity field is known, the stream function can be calculated. A streamline represents a line along which the stream function has a constant value, and a tangent drawn at any point of a streamline represents the direction of the local velocity vector. Figures 10(a) and 10(b) show a few illustrative streamlines obtained by the above-mentioned post-processing operations of present CFD simulations, respectively, for a Newtonian fluid (Bn = 0) and a Bingham fluid (Bn = 50). Each Figure contains three streamlines which start from $\Re$ = 10, $\Re$ = 30, and $\Re$ = 50. All the streamlines (in Figure 10) are shown up to $\Re$ = 110. The radial locations for the start and end points of the streamlines are selected arbitrarily for illustrating certain features. Two characteristics which are common in the shape for all the streamlines are as follows.

1. At large ζ (that is far from the disc-surface), the streamlines are approximately parallel to the axis of rotation.
2. At small ζ (that is near the disc-surface), the streamlines are spiral-shaped.

There are fluid dynamic reasons behind such shape of the streamlines. At large ζ, the axial velocity component is the only nonzero component of the velocity vector (because both radial and tangential velocity components asymptotically approach to zero at large ζ). Therefore, there the streamlines are parallel to the axis of rotation. Near the disc, the three components of velocity vector exist simultaneously. The streamlines are deflected radially outward due to the radial velocity and the streamlines are deflected in circumferential direction due to the tangential velocity. These two deflections result into streamline bending (see Figure 10). The spiral shape is attained because of the simultaneous existence of both radial and tangential components. The end of the spiral always shifts towards the disc due to the negative value of axial velocity. Thus, near the disc-surface, the streamlines take a conical helix shape.

Figure 10(b) (for Bn = 50) shows that a fluid streamline close to the disc-surface makes more number of complete turns around the axis of rotation. This is so because the radial velocity close to the disc-surface is much lower in the Bingham fluid as compared to the Newtonian fluid, whereas the tangential velocity is of comparable magnitude (slightly greater for a Bingham fluid) in the two cases [see Figures 3 and 4].

The values of ζ at $\Re$ = 110 for all streamlines shown in Figure 10 are mentioned in the figure caption. $\Re$ = 110 is selected as the end location for all streamlines only for illustrative purposes. For both Newtonian and Bingham fluids, it can be observed that the ζ-value at $\Re$ = 110 increases when a streamline starts from a greater value of $\Re$. For example, at $\Re$ = 110, the ζ-value of the

This article is copyrighted as indicated in the article. Reuse of AIP content is subject to the terms at: http://scitation.aip.org/termsconditions. Downloaded to IP: 203.110.246.23 On: Sun, 10 Jan 2016 14:27:14

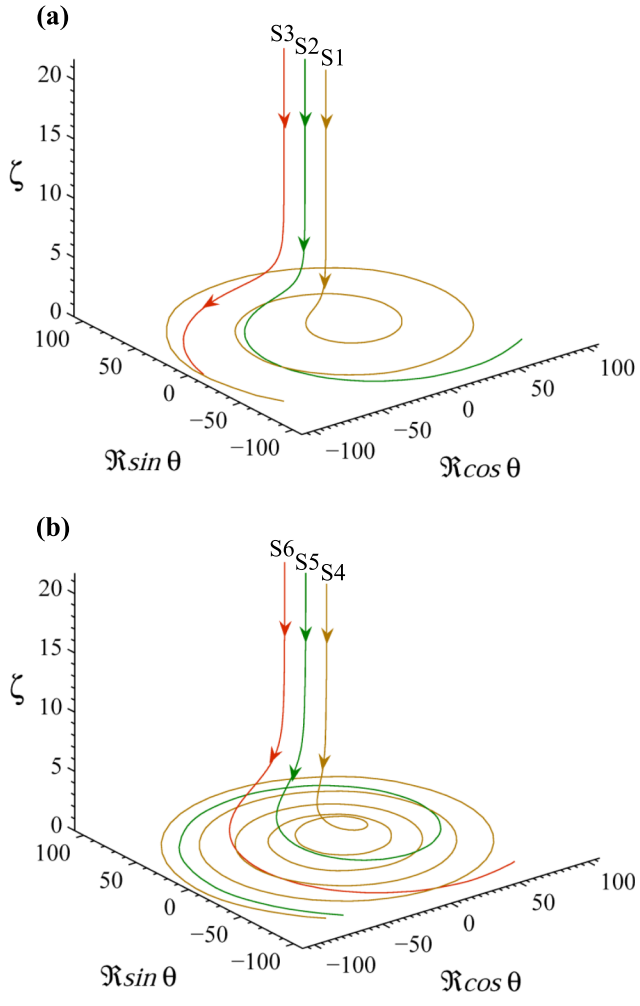

FIG. 10. Streamlines obtained from the present CFD simulation for Newtonian and Bingham fluids. (a) Computed streamlines for a Newtonian fluid ($Bn = 0$); (b) computed streamlines for a Bingham fluid ($Bn = 50$). $(\Re, \zeta)$ co-ordinates of the beginning and end of each streamline: S_1 [(10, 21.7) → (110, 0.12)]; S_2 [(30, 21.7) → (110, 0.41)]; S_3 [(50, 21.7) → (110, 0.77)]; S_4 [(10, 21.7) → (110, 0.11)]; S_5 [(30, 21.7) → (110, 0.36)]; S_6 [(50, 21.7) → (110, 0.73)].

streamline which originates at $\Re = 10$ is less as compared to the ζ-value of the streamline which originates at $\Re = 50$, i.e., the vertical displacement of a fluid particle is less in the second case (for steady state, a streamline is the same as a pathline). These results may, at the first glance, seem to be inconsistent with the fact that the magnitude of axial velocity increases with an increase in $\Re$ as shown in Figure 6(c). The paradox regarding why the vertical displacement of a fluid particle, which moves with a greater axial velocity (in the ζ-direction), would be lower can be resolved when one considers that the time taken by the two fluid particles to reach the final location at $\Re = 110$ is not the same. A fluid particle which follows the streamline starting from $\Re = 10$ takes more time to reach at $\Re = 110$ as compared to a fluid particle which follows the streamline starting from $\Re = 50$. The time, which a fluid particle needs to reach at $\Re = 110$, depends on the radial distance and average radial velocity (Figure 6(b) shows that the radial velocity increases with radius). Greater radial distance and smaller average radial velocity are the causes for which a fluid particle starting from $\Re = 10$ requires more time to reach at $\Re = 110$.

E. Non-similar solutions versus self-similar solutions

The classical solution given by von Kármán for the flow of a Newtonian fluid above a rotating disc exhibits similarity. For the existence of similarity, the axial variations of the non-dimensional

This article is copyrighted as indicated in the article. Reuse of AIP content is subject to the terms at: http://scitation.aip.org/termsconditions. Downloaded to IP: 203.110.246.23 On: Sun, 10 Jan 2016 14:27:14

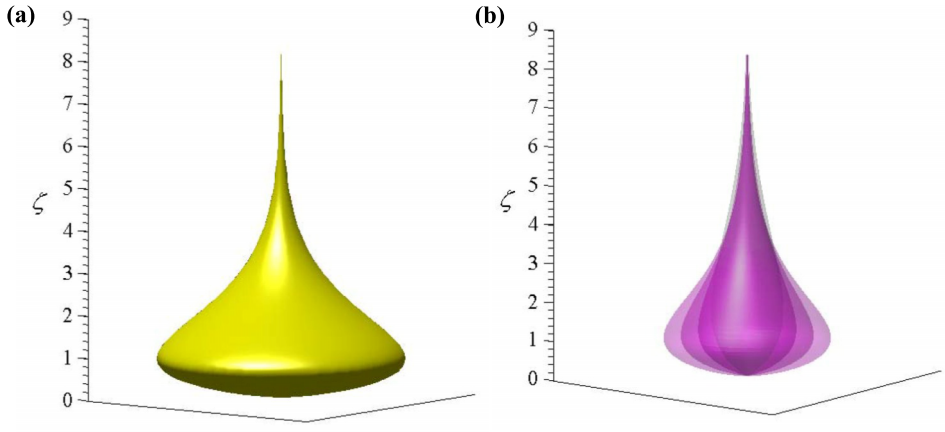

FIG. 11. (a) An artist's impression of the top-like structure of the self-similar radial velocity profiles in a Newtonian fluid (b) An artist's impression of the onion-like structure of the non-similar radial velocity profiles in a Bingham fluid ($Bn = 50$).

velocity-components are independent of *Re* (in this paper, flow is considered to be laminar). The present study shows that similarity does not hold for the flow of a Bingham fluid above a rotating disc. The differences between the non-similar solution of a Bingham fluid and the self-similar solution of a Newtonian fluid are shown in this section.

Figure 11 shows the axial variations of non-dimensional radial velocity ($\hat{V}_r$-profiles) for Newtonian and Bingham fluids over a large range of non-dimensional radius ℜ. Figure 11(a) corresponds to the flow of a Newtonian fluid and Figure 11(b) corresponds to the flow of a Bingham fluid ($Bn = 50$). The flow field is axi-symmetric in both cases; therefore, it is possible to obtain surfaces of revolution by integrating the $\hat{V}_r$-profiles. For a Newtonian fluid, the $\hat{V}_r$-profiles over a large range of ℜ superpose on one another due to the existence of similarity. This results into a single surface of revolution. Figure 11(a) shows that this surface of revolution takes a top-like structure. For a Bingham fluid, the $\hat{V}_r$-profiles over a large range of ℜ does not superpose on one another because of non-similarity. This results in the existence of many surfaces of revolution over a range of ℜ. Figure 11(b) is composed of four such surfaces of revolutions. The surfaces are at ℜ = 5, ℜ = 30, ℜ = 60, and ℜ = 110. Figure 11(b) shows that a combination of the surfaces can be represented as an onion-like structure in which each surface is a shell of this onion (though at large ζ, the surfaces may cross).

The non-similarity in the flow-field of a Bingham fluid can be examined with another example. Figures 12(a) and 12(b) show the distributions of non-dimensional axial velocity ($\hat{V}_z$) for a Newtonian fluid ($Bn = 0$) and for a Bingham fluid ($Bn = 50$), respectively, obtained by CFD.

For a particular ζ, a Newtonian fluid shows no change in $\hat{V}_z$ over a large range of ℜ due to the existence of similarity. The computed $\hat{V}_z$ is found to be a function only of ζ and not of ℜ, as was the case in von Kármán's solution. The iso-$\hat{V}_z$ surfaces of Figure 12(a) are all parallel to the ℜ-axis, demonstrating the accuracy of the CFD simulations. This monolithic simplicity of the iso-$\hat{V}_z$ surfaces of Figure 12(a) disappears when one plots the contours of $\hat{V}_z$ for a Bingham fluid shown in Figure 12(b). For a particular ζ, $\hat{V}_z$ of a Bingham fluid varies with ℜ due to non-similarity, $|\hat{V}_z|$ increasing with an increase in ℜ. The iso-$\hat{V}_z$ surfaces for a Bingham fluid appear L-shaped on the ℜ-ζ plane.

F. Limiting behaviours of the solutions and exploration for possible scaling

For a Newtonian fluid, *Bn* is zero. Equations (17)–(19) take the following form in the limit $Bn \to 0$:

This article is copyrighted as indicated in the article. Reuse of AIP content is subject to the terms at: http://scitation.aip.org/termsconditions. Downloaded to IP: 203.110.246.23 On: Sun, 10 Jan 2016 14:27:14

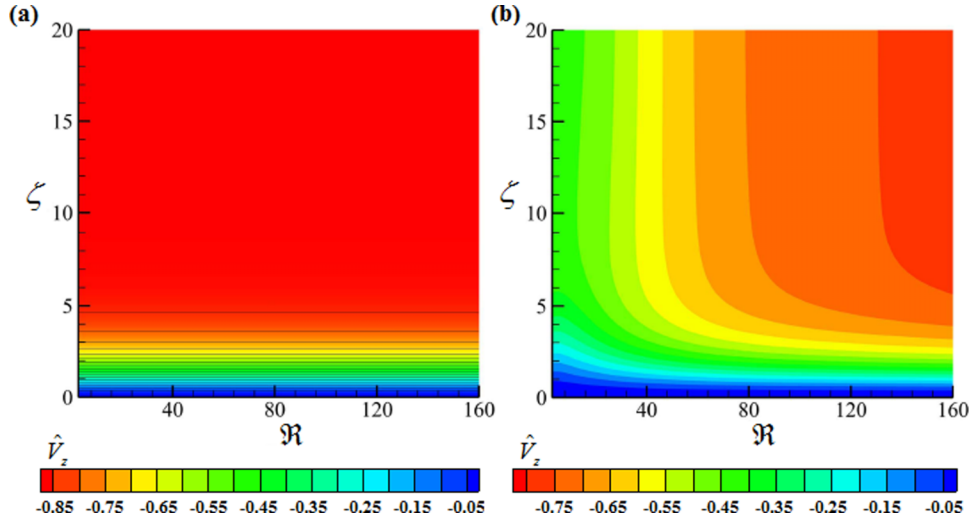

FIG. 12. The contours of non-dimensional axial velocity ($\hat{V}_z$) obtained from the present CFD simulations. (a) Self-similar $\hat{V}_z$-contour for a Newtonian fluid ($Bn = 0$); (b) non-similar $\hat{V}_z$-contour for a Bingham fluid ($Bn = 50$).

$$2\hat{V}_r + \hat{V}_z' = 0, \tag{41}$$

$$\hat{V}_r^2 - \hat{V}_\theta^2 + \hat{V}_z\hat{V}_r' = \hat{V}_r'', \tag{42}$$

$$2\hat{V}_r\hat{V}_\theta + \hat{V}_z\hat{V}_\theta' = \hat{V}_\theta''. \tag{43}$$

The single and double prime signs in Equations (41)–(43) represent, respectively, the first and second derivatives with respect to ζ. Equations (41)–(43), which are obtained as a limiting case of the equations for a Bingham fluid, are the same as the governing equations for the flow of a Newtonian fluid above a rotating disc (as given by von Kármán).

Now, for any positive but finite value of Bn, consider another limiting case when Re tends to infinity. Under this condition, it can be shown that Equations (17)–(19) again reduce to Equations (41)–(43). In other words, Equations (41)–(43) are obtained from Equations (17)–(19) either when $Bn \to 0$ or when $Re \to \infty$. We could not find any of the previous literature mentioning the implication of the limit $Re \to \infty$ for a Bingham fluid.

Thus, a Bingham fluid (for any positive but finite value of Bn) shows Newtonian behaviour at $Re \to \infty$. The mathematical infinity can, in practice, be replaced by a finite number which depends on the value of Bn. It can be shown from Equations (17)–(19) that the value of this finite number increases with an increase in Bn. When Bn tends to zero, a Bingham fluid becomes Newtonian at very small Re.

A few additional considerations would be relevant here. First of all, replacing the mathematical infinity ($Re \to \infty$) by a large but finite value of Re is also consistent with the requirement that for a laminar analysis to remain valid, the Reynolds number must be below the transition value (about 10^5 for a Newtonian fluid). Secondly, the physical implication of $Re \to \infty$ is not that viscous stresses are negligible with respect to inertial terms and consequently there is no discernible difference in the behaviour of a Bingham and a Newtonian fluid (since their difference lies in the quantification of the viscous term). It should be realized that both von Kármán's original formulation and the present formulation deal with rotational boundary layers inside which the viscous stresses are not negligible. That the viscous stresses do not vanish can be mathematically appreciated from the fact that in the limit $Re \to \infty$ for a Bingham fluid, the right hand sides of Equations (42) and (43) are non-zero. The second derivative terms $\hat{V}_r''$ and $\hat{V}_\theta''$ in Equations (42) and (43) are the viscous terms, and they are the same either for a Newtonian fluid or for a Bingham fluid with finite Bn and at $Re \to \infty$. Thirdly, the ζ-profile of $\hat{V}_r$ results from the application of the no-slip boundary condition on the disc surface, thus confirming once again that the solutions are viscous in nature. Fourthly, an additional physical insight may be obtained by considering the ratio Re/Bn, which is physically

This article is copyrighted as indicated in the article. Reuse of AIP content is subject to the terms at: http://scitation.aip.org/termsconditions. Downloaded to IP: 203.110.246.23 On: Sun, 10 Jan 2016 14:27:14

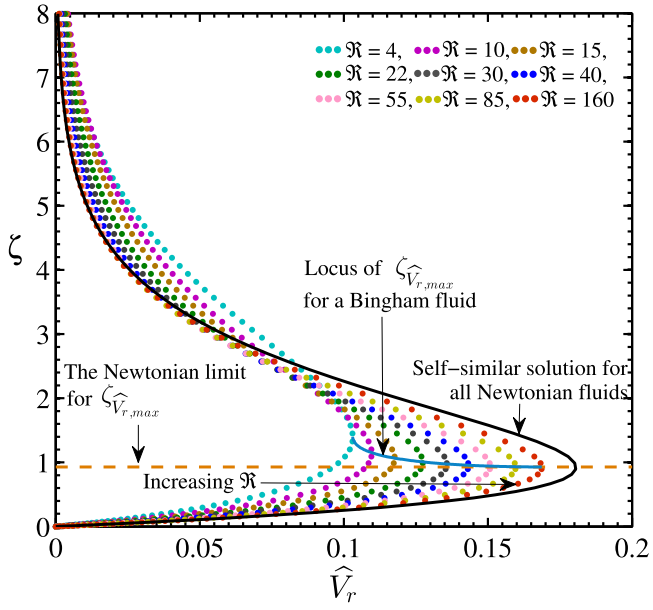

FIG. 13. Non-dimensional radial velocity ($\hat{V}_r$) profiles at various $\Re$ for a Bingham fluid (with $Bn = 10$) and their progressive development with an increase in $\Re$ towards the $\hat{V}_r$-profile of a Newtonian fluid.

related to the ratio of inertia to yield stress τ_y. For finite Bn, the condition $Re \to \infty$ implies that $Re/Bn \to \infty$. This means that, as compared to the inertia, the effect of the yield stress becomes negligible. The fluid behaviour then simply can be modelled by an equivalent Newtonian fluid with viscosity equal to μ_p. This interpretation also implies that as Bn increases, the convergence with Reynolds number, of the Bingham solutions to the Newtonian solution, would be slow.

The Newtonian limit for a Bingham fluid can also be demonstrated with the results of the present CFD simulations. At $Bn = 10$, the axial variation of $\hat{V}_r$ for various values of $\Re$ are calculated from CFD simulations. Figure 13 shows these calculated $\hat{V}_r$-profiles. The same figure also shows the unique $\hat{V}_r$-profile corresponding to a Newtonian fluid. ζ is plotted as the ordinate so that the vertical sense is retained for easy physical interpretation. The ζ vs. $\hat{V}_r$ profiles for a Bingham fluid are different for different values of $\Re$, whereas the ζ vs. $\hat{V}_r$ profile for a Newtonian fluid is independent of $\Re$. It is to be remembered that, for the rotating disc problem, Equation (10) shows that the non-dimensional radius and the Reynolds number are connected through the relation $\Re = r/\sqrt{\nu_p/\Omega} = \sqrt{Re}$. With an increase in $\Re$, the progressive development of the $\hat{V}_r$-profiles of Bingham fluid towards the unique Newtonian-$\hat{V}_r$-profile can be observed in Figure 13.

Figure 13 shows that the $\hat{V}_r$-profile corresponding to a particular $\Re$ has a maxima. In this paper, the maximum value of $\hat{V}_r$ is denoted as $\hat{V}_{r,\,max}$. The value of ζ corresponding to a $\hat{V}_{r,\,max}$ is denoted as $\zeta_{\hat{V}_{r,\,max}}$. It can be seen from Figure 13 that, for a Bingham fluid, both $\hat{V}_{r,\,max}$ and $\zeta_{\hat{V}_{r,\,max}}$ vary with $\Re$. For a Newtonian fluid, von Kármán's solution shows that $\hat{V}_{r,\,max} = 0.1808$ and $\zeta_{\hat{V}_{r,\,max}} = 0.93$, and that these values do not depend on the radius. The present CFD solutions also produce exactly the same results for a Newtonian fluid, thus lending further support to the accuracy of the present computations.

In order to understand how $\hat{V}_{r,\,max}$ and $\zeta_{\hat{V}_{r,\,max}}$ vary with $\Re$ for a Bingham fluid, the results of many CFD simulations have been post-processed to extract the variations of $\hat{V}_{r,\,max}$ and $\zeta_{\hat{V}_{r,\,max}}$ with $\Re$. The outcome of these computations has been displayed in Figures 14 and 15. The figures additionally provide graphical demonstration of the newly enunciated physical principle that all Bingham fluids (with finite Bn) behave like a Newtonian fluid at sufficiently large values of Re.

Figure 14 shows $\hat{V}_{r,\,max}$ versus $\Re$ for various values of Bn. The same figure also shows the Newtonian limit for $\hat{V}_{r,\,max}$ (0.1808) that is the maximum possible value of $\hat{V}_{r,\,max}$ for the flow of a Bingham fluid above a rotating disc. As $\Re$ increases, for a particular Bn, $\hat{V}_{r,\,max}$ at first (in a

This article is copyrighted as indicated in the article. Reuse of AIP content is subject to the terms at: http://scitation.aip.org/termsconditions. Downloaded to IP: 203.110.246.23 On: Sun, 10 Jan 2016 14:27:14

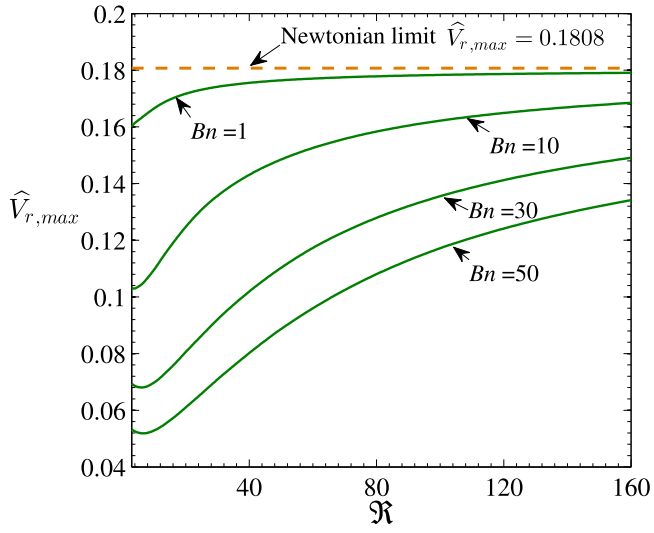

FIG. 14. Variation of $\hat{V}_{r,\,max}$ (maximum non-dimensional radial velocity at any particular $\Re$) with non-dimensional radius $\Re$ for various *Bn*. [For all *Bn*, $\hat{V}_{r,\,max}$ for a Bingham fluid approaches towards $\hat{V}_{r,\,max}$ of a Newtonian fluid with an increase in $\Re$.]

region close to the axis of rotation) decreases and then onwards increases, the rate of increase of $\hat{V}_{r,\,max}$ decreasing with $\Re$. For a particular $\Re$, $\hat{V}_{r,\,max}$ decreases with an increase in *Bn*. Figure 14 clearly shows that the curve (of $\hat{V}_{r,\,max}$-$\Re$) corresponding to *Bn* = 1 asymptotically approaches the Newtonian limit for $\hat{V}_{r,\,max}$. Figure 14 also shows that with an increase in *Bn*, the $\hat{V}_{r,\,max}$-$\Re$ curves will attain the Newtonian limit at a greater value of $\Re$.

Figure 15 shows the variation of $\zeta_{\hat{V}_{r,\,max}}$ (non-dimensional axial coordinate corresponding to $\hat{V}_{r,\,max}$) with respect to $\Re$ for various *Bn*. The Newtonian limit for $\zeta_{\hat{V}_{r,\,max}}$, as shown in Figure 15, is 0.93. As $\Re$ increases, for a particular *Bn*, $\zeta_{\hat{V}_{r,\,max}}$ generally decreases, the rate of decrease of $\zeta_{\hat{V}_{r,\,max}}$ decreasing with $\Re$. For a particular $\Re$, $\zeta_{\hat{V}_{r,\,max}}$ increases with an increase in *Bn*. It can be observed how the $\zeta_{\hat{V}_{r,\,max}}$ vs. $\Re$ curve corresponding to *Bn* = 10 asymptotically approaches the Newtonian

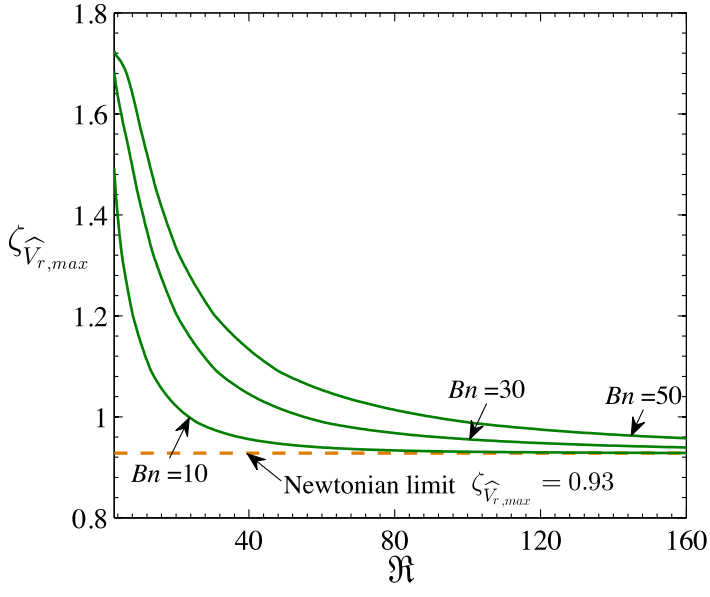

FIG. 15. Variation of $\zeta_{\hat{V}_{r,\,max}}$ (non-dimensional axial coordinate corresponding to $\hat{V}_{r,\,max}$) with non-dimensional radius $\Re$ for various *Bn*. [For all *Bn*, $\zeta_{\hat{V}_{r,\,max}}$ for a Bingham fluid approaches towards $\zeta_{\hat{V}_{r,\,max}}$ of a Newtonian fluid with an increase in $\Re$.]

This article is copyrighted as indicated in the article. Reuse of AIP content is subject to the terms at: http://scitation.aip.org/termsconditions. Downloaded to IP: 203.110.246.23 On: Sun, 10 Jan 2016 14:27:14

limit. [The curve corresponding to $Bn = 1$ reaches the Newtonian limit at a smaller value of $\Re$; but the curve is not shown in this figure for avoiding data congestion.] A comparison between Figures 14 and 15 shows that, corresponding to a particular Bn, the Newtonian limit for $\zeta_{\hat{V}_{r,\,max}}$ is reached at a lower value of $\Re$ as compared to the radial location where the Newtonian limit for $\hat{V}_{r,\,max}$ is reached. As an example, for $Bn = 10$, Figure 15 shows that the Newtonian limit for $\zeta_{\hat{V}_{r,\,max}}$ is nearly reached at $\Re = 160$, but Figure 14 shows that the Newtonian limit for $\hat{V}_{r,\,max}$ will be reached at much greater value of $\Re$. If one studies the locus of $\zeta_{\hat{V}_{r,\,max}}$ in Figure 13 vis-à-vis the approach of $\hat{V}_{r,\,max}$ towards their respective Newtonian limits, then also it becomes clear that, along the $\Re$ axis, $\zeta_{\hat{V}_{r,\,max}}$ reaches the Newtonian limit before $\hat{V}_{r,\,max}$ does so.

We explored the idea whether it is possible to define a composite non-dimensional number involving Bn and Re such that new scaling of solutions would be possible. Our efforts to find any direct utility of the simple ratio of Bn and Re failed since strong non-linearity is present in the variation of Bingham solutions with Bn at a fixed Re or *vice versa*. Taking cue from Equation (15), we therefore tried to discover any special physical meaning of the non-linear combination Re^m/Bn in unifying the various curves contained in Figures 14 and 15. This effort has met with partial success, the outcome is depicted in Figure 16.

G. Representation of the boundary-layer surface

It has been discussed in Section V A that $\hat{V}_\theta$ (non-dimensional tangential velocity) is maximum at the disc-surface where it equals 1; $\hat{V}_\theta$ decreases with an increase in ζ, and far from the disc, $\hat{V}_\theta$ asymptotically approaches to zero. As per convention,[2] a boundary-layer thickness is defined to be the axial distance away from the rotating disc at which $\hat{V}_\theta$ equals 0.01. The axi-symmetric surface, which corresponds to $\hat{V}_\theta = 0.01$, is referred in the present study as the boundary-layer surface. The boundary-layer surfaces are calculated by using CFD over a large range of $\Re$. Figure 17 shows boundary-layer surfaces for various Bn (Bn equals 0, 10, 30, and 50).

Figure 17(a) shows that the boundary-layer surface for a Newtonian fluid ($Bn = 0$) is flat. This indicates that, for laminar flow, the non-dimensional boundary-layer thickness ($\hat{\delta} \equiv \delta/\sqrt{\nu_p/\Omega}$) of a Newtonian fluid is independent of $\Re$. Theory[2] shows that the value of $\hat{\delta}$ for a Newtonian fluid is 5.5 which is the same value obtained from the present CFD simulation as shown in Figure 17(a). The absolute flatness of the computed surface shown in Figure 17(a) gives confidence in the accuracy of the numerical results.

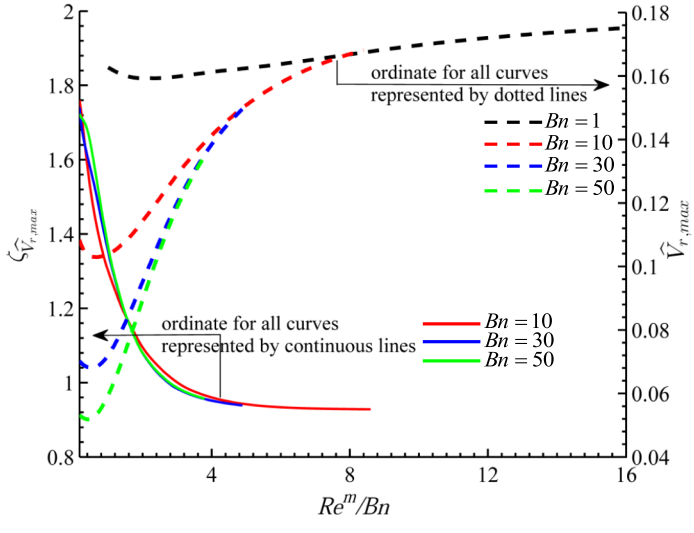

FIG. 16. Variations of $\hat{V}_{r,\,max}$ and $\zeta_{\hat{V}_{r,\,max}}$ with Re^m/Bn obtained by the present CFD simulations for various values of Bn (the values of m are calculated by Equation (15)).

This article is copyrighted as indicated in the article. Reuse of AIP content is subject to the terms at: http://scitation.aip.org/termsconditions. Downloaded to IP: 203.110.246.23 On: Sun, 10 Jan 2016 14:27:14

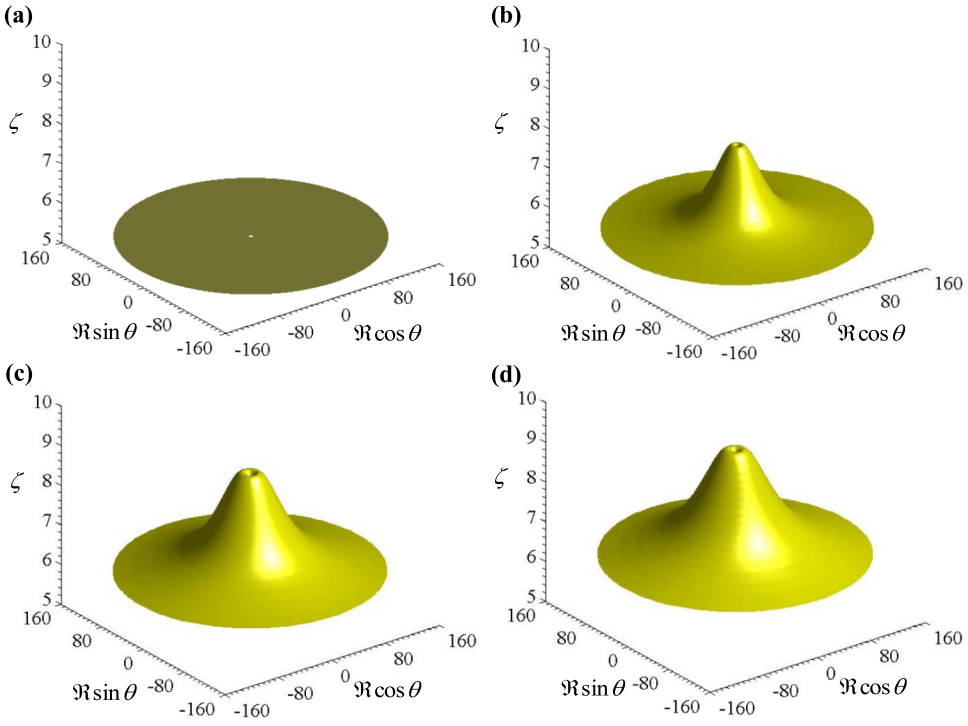

FIG. 17. Variation of non-dimensional boundary-layer thickness with $\Re$ obtained from the present CFD simulations for Newtonian and Bingham fluids. (a) $Bn = 0$ (Newtonian fluid); (b) $Bn = 10$; (c) $Bn = 30$; (d) $Bn = 50$. (Minimum value of $\Re$ considered in the above representations is 2.67.)

Figures 17(b)–17(d) show the boundary-layer surfaces for Bn = 10, Bn = 30, and Bn = 50, respectively. Figure 18 shows the finer details of the shape of the surfaces at low value of $\Re$ (i.e., close to the axis of rotation). It can be observed that, in contrast to what happens in a Newtonian fluid, $\hat{\delta}$ for a Bingham fluid is a complex function of $\Re$. Although the boundary-layer thickness generally increases with a decrease in $\Re$ when $\Re$ is relatively large (Figure 17), it eventually decreases as one approaches the axis of rotation (Figure 18). The subtle behaviour close to the axis of rotation is not perceptibly captured on the scale used for Figure 17 (so this region is discussed separately later). According to Figures 17(b)–17(d), boundary-layer surfaces corresponding to Bingham fluids obtain hat-like structure. The central portions of the surfaces are peaky, and, the surfaces gradually become disc-shaped with an increase in $\Re$. It has been discussed in Section V F that a Bingham fluid behaves like a Newtonian fluid at large $\Re$. For example, Figure 17(b) shows that when $\Re$ is greater than 100, the boundary-layer surface takes a disc-like shape, and $\hat{\delta}$ approaches to 5.5 (Newtonian limit). The shapes of the boundary layer surfaces shown in Figures 17(b)–17(d) are related to the corresponding morphology of the unyielded zone.

A possible explanation for the increase of $\hat{\delta}$ with a decrease in $\Re$, as shown in Figures 17(b)–17(d), is as follows. Consider two fluid particles at $\Re_1$ and $\Re_2$ on a particular ζ-plane above a rotating disc. Suppose $\Re_2$ is greater than $\Re_1$. For a Newtonian fluid, $\hat{V}_\theta$ is independent of $\Re$ due to self-similar solution. So, for a Newtonian fluid, $\hat{V}_\theta$ at $\Re_1$ ($\hat{V}_{\theta,1N}$) and $\hat{V}_\theta$ at $\Re_2$ ($\hat{V}_{\theta,2N}$) are equal, and an iso-ζ plane is equivalent to an iso-$\hat{V}_\theta$ plane. However, for a Bingham fluid, $\hat{V}_\theta$ at $\Re_1$ ($\hat{V}_{\theta,1B}$) is not equal to $\hat{V}_\theta$ at $\Re_2$ ($\hat{V}_{\theta,2B}$) because of non-similarity. Now, consider an $\Re_2$ which is substantially large. According to Section V F, $\hat{V}_{\theta,2B}$ tends to $\hat{V}_{\theta,2N}$. Figure 3 shows that $\hat{V}_\theta$ at a particular $\Re$ increases with an increase in Bn. When $\Re_1$ is not large, $\hat{V}_{\theta,1B}$ will be greater than $\hat{V}_{\theta,1N}$ (or correspondingly greater than $\hat{V}_{\theta,2N}$). Therefore, for a Bingham fluid, to obtain an iso-$\hat{V}_\theta$-plane which passes through the coordinate of the second particle, ζ-coordinate of the first particle needs to be varied such that $\hat{V}_\theta$ decreases. Figure 3 shows that $\hat{V}_\theta$ decreases with an increase in ζ. Hence, to obtain an iso-$\hat{V}_\theta$-plane, ζ of the first particle should be greater than ζ of the second particle.

This article is copyrighted as indicated in the article. Reuse of AIP content is subject to the terms at: http://scitation.aip.org/termsconditions. Downloaded to IP: 203.110.246.23 On: Sun, 10 Jan 2016 14:27:14

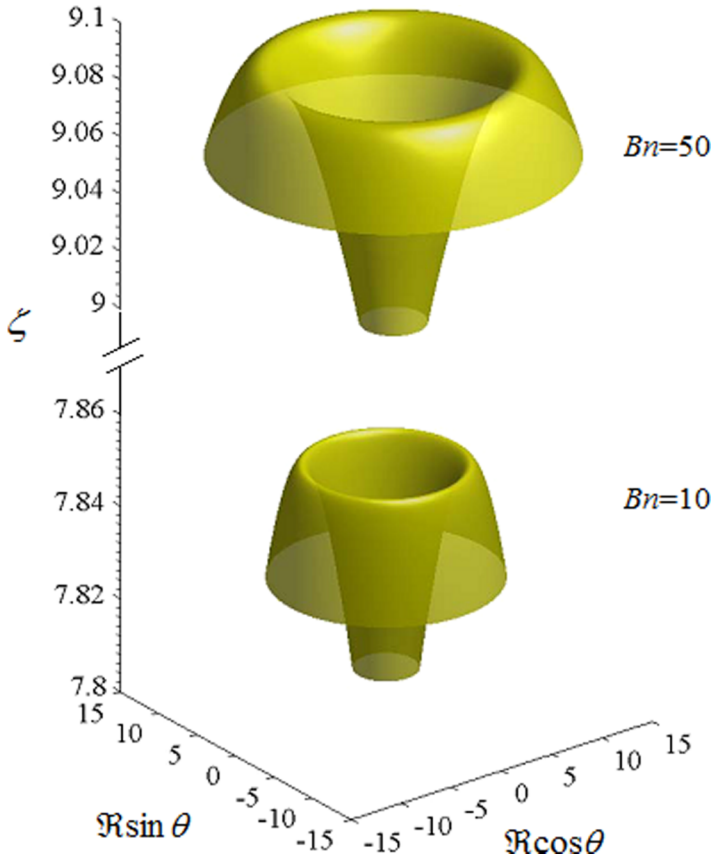

FIG. 18. Close-up view of non-dimensional boundary-layer thickness at low $\Re$ for Bingham fluids with $Bn = 10$ and $Bn = 50$. (Minimum value of $\Re$ considered in the above representations is 2.67.)

Figure 18 shows peculiar shapes of the computed boundary-layer surfaces obtained for small $\Re$ (of the order of 10). It can be observed that for small $\Re$, the boundary-layer thickness decreases, instead of increasing, with a decrease in $\Re$. Thus, at any Bn, a maxima for $\hat{\delta}$ is observed. Figure 18 shows that the location of the maxima shifts to greater $\Re$ when Bn increases. Nonlinearity of tangential velocity in the radial direction is the cause of the typical shape of the boundary-layer surfaces. The solutions obtained from both the CFD simulation and the semi-analytical model exhibit nonlinearity in the radial direction when Bn is greater than zero. At this point, it should be mentioned that the nonlinearity of the velocity-components in the axial direction is common to both Newtonian and Bingham fluids.

Our objective is to produce accurate solutions. One needs to be particularly careful while obtaining solutions close to the axis of rotation. Other than comparing the CFD and analytical solutions, we have taken a number of special steps to ensure the accuracy. A proper grid independence study is conducted (Section III C) and a stringent convergence criterion is specified (Section III A) in which the limit for the maximum residual for all conserved variables is set at 10^{-7} (which is smaller than that in many reported studies in CFD). Secondly, we set a critical query regarding what happens to the axial velocity V_z exactly at the axis of rotation and whether the 'axis boundary condition' of Fluent reproduces that correctly; the summary of the affirmative findings is given in the Appendix. Thirdly, we wanted to ensure that our solutions, particularly that close to the axis of rotation, are not dependent on our choice of μ_y in the bi-viscosity model (see Section III B where we have set the value of μ_y/μ_p to 50 000 for all computations reported in this paper). The Appendix contains the summary of a systematic sensitivity study and provides the justification for our choice of μ_y.

This article is copyrighted as indicated in the article. Reuse of AIP content is subject to the terms at: http://scitation.aip.org/termsconditions. Downloaded to IP: 203.110.246.23 On: Sun, 10 Jan 2016 14:27:14

TABLE III. Comparisons between von Kármán's flow of a Newtonian fluid and von Kármán's flow of a Bingham fluid.

Newtonian fluid	Bingham fluid
1. Due to self-similarity, the non-dimensional velocity components are independent of Re (when $Re < Re_{cr}$). See Figures 11(a) and 12(a).	1. Due to non-similarity, the non-dimensional velocity components vary with Re. See Figures 11(b) and 12(b).
2. The contours of constant non-dimensional axial velocity on r-z plane are parallel lines to the disc. See Figure 12(a).	2. The contours of constant non-dimensional axial velocity on r-z plane form complex pattern. See Figure 12(b).
3. von Kármán assumed the variations of radial velocity (V_r) and tangential velocities (V_θ) are linear with radius, confirmed by present CFD. See Figures 11(a) and 17(a).	3. The present semi-analytical approach and CFD both show that the variations of V_r and V_θ with r are nonlinear. See Figures 11(b), 17(b)–17(d), and 18.
4. The fluid elements at the disc surface rotate with the angular speed Ω of the disc (no slip). The angular velocity of the fluid elements above the disc is not a function of r and decreases with z (thus becoming zero at $z \to \infty$).	4. The angular speed of fluid elements Ω_{fluid} is a function of both r and z. At a fixed r, Ω_{fluid} decreases from $\Omega_{surface}$ to zero as z changes from 0 to ∞. At a fixed z, Ω_{fluid} tries to be close to $\Omega_{surface}$ as $r \to 0$ and shows complex variation with increasing r.
5. Axi-symmetric surface representing the boundary layer is sheet-like and parallel to the disc. See Figure 17(a).	5. Axi-symmetric surface representing the boundary layer forms hat-like shape with complex three-dimensional shape near the disc-centre. The hat-like shape can be seen in Figures 17(b)–17(d) and the complex three-dimensional shape can be seen in Figure 18.
6. A Fluid streamline close the disc surface makes less number of complete turns around the axis of rotation. See Figure 10(a).	6. A fluid streamline close to the disc surface makes more number of complete turns around the axis of rotation. This is so because the radial velocity close to the disc-surface is much lower in the Bingham fluid as compared to the Newtonian fluid, whereas the tangential velocity is of comparable magnitude in the two cases. See Figure 10(b).
7. The analytical expression for non-dimensional moment coefficient $C_{m,\,r}$ for a Newtonian fluid as given in Ref. 2 is $C_{m,\,r} = -\pi\,\hat{V}'_\theta(0)/\sqrt{Re}$.	7. The analytical expression for non-dimensional moment coefficient for a Bingham fluid as deduced here in Equation (38) is $C_{m,\,r} = -4\pi\,\hat{V}'_\theta(0)\left[\frac{Bn}{3\sqrt{Re\{\hat{V}_r^2(0)+\hat{V}_\theta^2(0)\}}} + \frac{1}{4}\right]\frac{1}{\sqrt{Re}}$.
8. Equations (41)–(43) govern the flow. Equations (41)–(43) are obtained using von Kármán's similarity transformation i.e., $V_r = r\Omega\ F(\zeta)$, $V_\theta = r\Omega\, G(\zeta)$ and $V_z = \sqrt{\nu_p \Omega}\, H(\zeta)$.	8. Equations (17)–(19) govern the flow, validated against results of full CFD simulations. Equations (17)–(19) are deduced using Equation (14), the transformation proposed in the present paper. The present work has established that Equations (41)–(43) are obtained from Equations (17)–(19) either when $Bn \to 0$ or when $Re \to \infty$.

H. Newtonian fluid versus Bingham fluid

Some major differences and similarities between the flow of a Newtonian fluid and the flow of a Bingham fluid above a rotating disc, deduced in the present investigation, are brought together in Table III for ready reference.

VI. CONCLUSION

The Bingham fluid flow above a rotating disc has been investigated rigorously in three complementary but separate ways: (i) full CFD simulations and (ii) semi-analytical approach involving Equations (17)–(19), and (iii) semi-analytical approach involving Equations (28)–(30). In the CFD simulations, partial differential equations (1)–(4) are solved; whereas in the semi-analytical

This article is copyrighted as indicated in the article. Reuse of AIP content is subject to the terms at: http://scitation.aip.org/termsconditions. Downloaded to IP: 203.110.246.23 On: Sun, 10 Jan 2016 14:27:14

approach, ordinary differential equations (17)–(19) are solved. Equations (17)–(19) are obtained by simplifying Equations (1)–(4) invoking several assumptions and a new transformation law (Equation (14)). It is shown here that all three components of the velocity-field obtained by the semi-analytical approach are well-matched with the velocity-field obtained in the CFD simulations. Present deductions demonstrate that the new transformation law reduces to von Kármán's transformation as a limiting case ($yn \to 0$) and Equations (17)–(19) give rise to another set of ordinary differential equations (28)–(30). Figure 6 shows a comparison among the CFD solutions, numerical solutions of Equations (17)–(19) and numerical solutions of Equations (28)–(30). It has been observed that the predictions of the full CFD simulations are better estimated by Equations (17)–(19) than by Equations (28)–(30). Moreover, the present paper provides a closed-form analytical expression for predicting the non-dimensional moment coefficient $C_{m,\,r}$ (Equation (38)) which works well in comparison with values obtained by the full CFD simulations, as shown in Table II.

Some important fluid dynamic aspects can be observed in Figures 3–5 which show, respectively, the axial variations of $\hat{V}_\theta$, $\hat{V}_r$, and $\hat{V}_z$ at a moderate value of Re ($Re = 3000$) for various Bn. At a fixed Re, the $\hat{V}_\theta$ is maximum at the disc-surface (this maximum value is one) and asymptotically becomes zero at large ζ; the $|\hat{V}_z|$ is zero at the disc-surface and asymptotically attains its maximum at large ζ; the $\hat{V}_r$ is zero at the disc-surface and asymptotically becomes zero again at large ζ. In between, $\zeta = 0$ and $\zeta \to \infty$, $\hat{V}_\theta$ decreases; $|\hat{V}_z|$ increases; and $\hat{V}_r$ first increases to attain a maximum value and then decreases. With an increase in Bn, the maximum value in the $\hat{V}_r$-profile decreases; the ζ-value corresponding to the maximum $\hat{V}_r$ increases. $\hat{V}_r$-ζ profiles corresponding to any two Bn undergo a crossover. The decrease of maxima, the shift of maxima, and the crossover occur because of the effect of two opposing forces, viz. viscous force and inertial force. Some other important effects due to an increase in Bn (at a given Re and ζ) are the increase of $\hat{V}_\theta$ and the decrease of $|\hat{V}_z|$. The net radial outflow decreases due to the decrease of $|\hat{V}_z|$.

Figure 10 shows the differences in the characteristics between the streamlines in a Newtonian fluid flow and the streamlines in a Bingham fluid flow. For a Bingham fluid, a streamline close to the disc-surface makes more number of complete turns around the axis of rotation. This is so because the radial velocity close to the disc-surface is much lower in the Bingham fluid as compared to the Newtonian fluid, whereas the tangential velocity is of comparable magnitude in the two cases.

The present study shows that self-similarity does not hold for the flow of a Bingham fluid above a rotating disc. The differences between the self-similar solution of a Newtonian fluid and the non-similar solution of a Bingham fluid are illustrated by two examples as given in Figures 11 and 12. Figure 11(a) shows that for a Newtonian fluid, the $\zeta-$profiles of $\hat{V}_r$ at various $\mathfrak{R}$ are all superposed on one another. As a result, the surfaces of revolution obtained from the $\zeta-$ profiles of $\hat{V}_r$ form a top-like structure. On the other hand, Figure 11(b) shows that for a Bingham fluid, the $\zeta-$ profiles of $\hat{V}_r$ at various $\mathfrak{R}$ do not superpose resulting into an onion-like structure. Figure 12(a) shows that for a Newtonian fluid, the contours of constant non-dimensional axial velocity on $\mathfrak{R}$-ζ plane are parallel lines to the disc. On the other hand, Figure 12(b) shows that for a Bingham fluid, the contours of constant non-dimensional axial velocity on $\mathfrak{R}$-ζ plane form complex pattern.

Two limiting cases, viz. $Bn \to 0$ and $Re \to \infty$, are considered. The present results show that the Bingham fluid solution progressively approaches von Kármán's solution for a Newtonian fluid as the Bingham number is progressively reduced to zero ($Bn \to 0$). It is also established here that, for finite values of Bn, the Bingham fluid solution progressively approaches the von Kármán's solution for a Newtonian fluid as the non-dimensional radius and Reynolds number increase. The higher the value of Bn, the higher is the required value of Re at which convergence with the solution for Newtonian fluid occurs. It is shown in Figures 13–15 that $\hat{V}_{r,max}$ and $\zeta_{\hat{V}_{r,max}}$ for a Bingham fluid asymptotically approach to their corresponding Newtonian limits when Re is sufficiently large. A comparison between Figures 14 and 15 shows that, corresponding to a particular Bn, the Newtonian limit for $\zeta_{\hat{V}_{r,max}}$ is reached at a lower value of non-dimensional radius $\mathfrak{R}$ ($\mathfrak{R} = r/\sqrt{\nu_p/\Omega} = \sqrt{Re}$) as compared to the radial location where the Newtonian limit for $\hat{V}_{r,max}$ is reached. With an increase in $\mathfrak{R}$, the progressive development of the boundary layer surfaces for various Bn is captured in Figures 17 and 18. For a Newtonian fluid, the boundary layer surface is flat and sheet-like, whereas

This article is copyrighted as indicated in the article. Reuse of AIP content is subject to the terms at: http://scitation.aip.org/termsconditions. Downloaded to IP: 203.110.246.23 On: Sun, 10 Jan 2016 14:27:14

for a Bingham fluid, the boundary layer surface is hat-like (excluding the region near disc-centre where the boundary layer surface for a Bingham fluid forms complex three-dimensional shape; see Figure 18). Figure 17(b) clearly shows how the hat-like boundary layer surface, with an increase in $\mathfrak{R}$, turns into a sheet like surface and tries to attain $\zeta = 5.5$ (corresponding to the $\hat{\delta}$ for a Newtonian fluid). This provides further evidence for the existence of the Newtonian limits for a Bingham fluid.

APPENDIX: FURTHER COMPUTATIONS SHOWING THE SUITABILITY OF AXIS BOUNDARY CONDITION AND THE SUITABILITY OF THE CHOICE OF μ_y/μ_p IN THE BI-VISCOSITY MODEL

1. "Axis boundary condition" of Fluent

We implemented the "axis boundary condition" to reduce computational time since a large number of separate simulations were needed for the present study. In order to determine whether this boundary condition can produce accurate solutions, particularly very close to the axis of rotation, full three-dimensional computations were also undertaken for a Newtonian fluid and for representative Bingham numbers. These further computations showed that there is no discernible difference between the solutions of these carefully conducted full 3-D solutions and that reported in this paper.

Since obtaining the correct value of the axial velocity at the axis of rotation would be a critical test for the "axis boundary condition," only the ζ-profile of $\hat{V}_z$ at the centre of the disc is shown in Figure 19.

For brevity, only the comparison for a Newtonian fluid is shown. It can be seen that the computed results with 'axis boundary condition' agree well with the full 3-D computational results and von Kármán's analytical solution.

2. Choice of μ_y/μ_p in the bi-viscosity model

O'Donovan and Tanner[35] took $\mu_y/\mu_p = 1000$ and Turan *et al.*[32] took $\mu_y/\mu_p = 10\,000$. All computational results given in the main body of this paper are obtained with $\mu_y/\mu_p = 50\,000$.

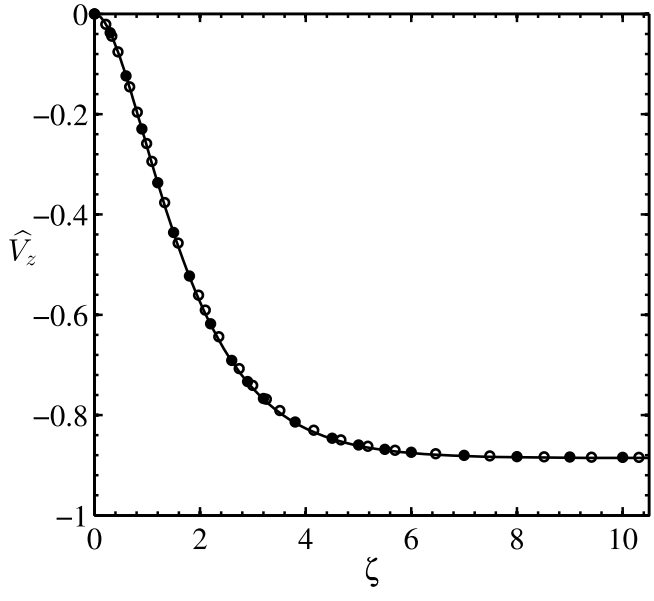

FIG. 19. Axial velocity at the centre of the disc: comparisons of ζ-variation of the non-dimensional axial velocity ($\hat{V}_z$) for a Newtonian fluid obtained by three different methods. (——) $\hat{V}_z$ obtained by three dimensional CFD simulation at the centre of the disc ($\mathfrak{R} = 0$); (○) $\hat{V}_z$ obtained by axisymmetric CFD simulation at the "axis boundary" (i.e., $\mathfrak{R} = 0$); (●) $\hat{V}_z$ determined by similarity solution.[39]

This article is copyrighted as indicated in the article. Reuse of AIP content is subject to the terms at: http://scitation.aip.org/termsconditions. Downloaded to IP: 203.110.246.23 On: Sun, 10 Jan 2016 14:27:14

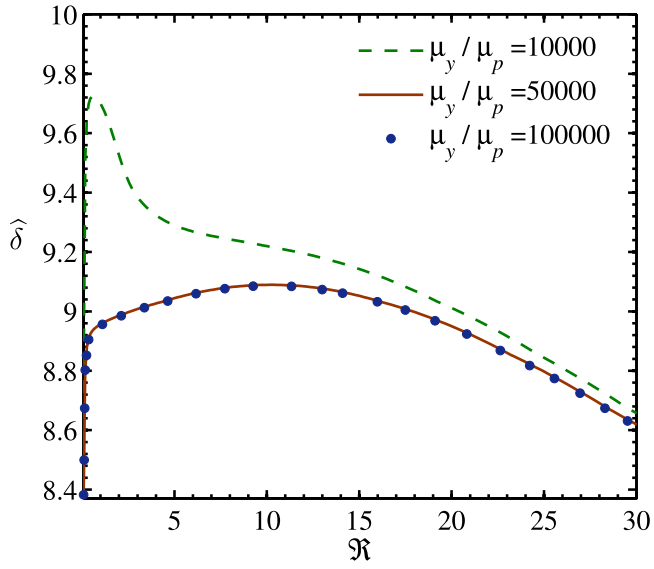

FIG. 20. Effect of varying μ_y/μ_p on the computed non-dimensional boundary-layer thickness ($\hat{\delta}$) in the proximity of disc-centre. [All calculations correspond to $Bn = 50$.]

Figure 20 depicts a sensitivity analysis on the choice of μ_y for the flow over a rotating disc. It can be seen that even doubling the value of μ_y/μ_p over the adopted value for the present study (50 000) does not appreciably change the solution, either qualitatively or quantitatively. However, the solution would be altered if $\mu_y/\mu_p = 10\,000$ or lower ratios are used.

[1] T. von Kármán, "Über Läminare und turbulence Reibung," Z. Angew. Math. Mech. **1**, 233–252 (1921).
[2] P. R. N. Childs, *Rotating Flow* (Butterworth-Heinemann, Oxford, UK, 2011).
[3] P. J. Zandbergen and D. Dijkstra, "Von Kármán swirling flows," Annu. Rev. Fluid Mech. **19**(1), 465–491 (1987).
[4] R. J. Lingwood, "Absolute instability of the Ekman layer and related rotating flows," J. Fluid Mech. **331**, 405–428 (1997).
[5] C. Davies and P. W. Carpenter, "Global behaviour corresponding to the absolute instability of the rotating-disc boundary layer," J. Fluid Mech. **486**, 287–329 (2003).
[6] M. Turkyilmazoglu, "Purely analytic solutions of the compressible boundary layer flow due to a porous rotating disk with heat transfer," Phys. Fluids **21**(10), 106104 (2009).
[7] C. Thomas and C. Davies, "Global stability of the rotating-disc boundary layer with an axial magnetic field," J. Fluid Mech. **724**, 510–526 (2013).
[8] Y. Burnishev and V. Steinberg, "Torque and pressure fluctuations in turbulent von Karman swirling flow between two counter-rotating disks. I," Phys. Fluids **26**(5), 055102 (2014).
[9] S. Poncet, M. P. Chauve, and P. Le Gal, "Turbulent rotating disk flow with inward throughflow," J. Fluid Mech. **522**, 253–262 (2005).
[10] R. J. Lingwood and S. J. Garrett, "The effects of surface mass flux on the instability of the BEK system of rotating boundary-layer flows," Eur. J. Mech., B: Fluids **30**(3), 299–310 (2011).
[11] A. Guha and S. Sengupta, "The fluid dynamics of the rotating flow in a Tesla disc turbine," Eur. J. Mech., B: Fluids **37**, 112–123 (2013).
[12] A. Guha and S. Sengupta, "The fluid dynamics of work transfer in the non-uniform viscous rotating flow within a Tesla disc turbomachine," Phys. Fluids **26**(3), 033601 (2014).
[13] G. K. Batchelor, "Note on a class of solutions of the Navier–Stokes equations representing steady rotationally-symmetric flow," Q. J. Mech. Appl. Math. **4**, 29–41 (1951).
[14] V. W. Ekman, "On the influence of the earth's rotation on ocean currents," Ark. Mat. Astron. Fys. **2**(11), 1–53 (1905).
[15] K. Stewartson, "On the flow between two rotating coaxial disks," Proc. Cambridge Philos. Soc. **49**, 333–341 (1953).
[16] N. S. Berman and M. A. Pasch, "Laser doppler velocity measurements for dilute polymer solutions in the laminar boundary layer of a rotating disk," J. Rheol. **30**(3), 441–458 (1986).
[17] A. Acrivos, M. J. Shah, and E. E. Petersen, "On the flow of a non-Newtonian liquid on a rotating disk," J. Appl. Phys. **31**(6), 963–968 (1960).
[18] H. I. Andersson, E. De Korte, and R. Meland, "Flow of a power-law fluid over a rotating disk revisited," Fluid Dyn. Res. **28**(2), 75–88 (2001).
[19] C. Ming, L. Zheng, and X. Zhang, "Steady flow and heat transfer of the power-law fluid over a rotating disk," Int. Commun. Heat Mass Transfer **38**(3), 280–284 (2011).
[20] A. M. Siddiqui, A. A. Farooq, T. Haroon, and B. S. Babcock, "A variant of the classical Von Kármán flow for a Jeffrey fluid," Appl. Math. Sci. **7**(20), 983–991 (2013).

This article is copyrighted as indicated in the article. Reuse of AIP content is subject to the terms at: http://scitation.aip.org/termsconditions. Downloaded to IP: 203.110.246.23 On: Sun, 10 Jan 2016 14:27:14

[21] L. Elliott, "Elastico-viscous flow near a rotating disk," Phys. Fluids **14**(6), 1086–1090 (1971).
[22] D. D. Kale, R. A. Mashelkar, and J. Ulbrecht, "Rotational viscoelastic laminar boundary layer flow around a rotating disc," Rheol. Acta **14**(7), 631–640 (1975).
[23] P. D. Ariel, "On the flow of an elastico-viscous fluid near a rotating disk," J. Comput. Appl. Math. **154**(1), 1–25 (2003).
[24] N. Dubash and I. Frigaard, "Conditions for static bubbles in viscoplastic fluids," Phys. Fluids **16**(12), 4319–4330 (2004).
[25] C. Ancey, N. J. Balmforth, and I. Frigaard, "Visco-plastic fluids: From theory to application," J. Non-Newtonian Fluid Mech. **158**(1), 1–3 (2009).
[26] N. J. Balmforth, I. A. Frigaard, and G. Ovarlez, "Yielding to stress: Recent developments in viscoplastic fluid mechanics," Annu. Rev. Fluid Mech. **46**, 121–146 (2014).
[27] E. C. Bingham, "An investigation of the laws of plastic flow," U.S. Bur. Stand. Bull. **13**, 309–353 (1916).
[28] A. A. Rashaida, D. J. Bergstrom, and R. J. Sumner, "Mass transfer from a rotating disk to a Bingham fluid," Trans. ASME: J. Appl. Mech. **73**, 108–111 (2006).
[29] A. Ahmadpour and K. Sadeghy, "Swirling flow of Bingham fluids above a rotating disk: An exact solution," J. Non-Newtonian Fluid Mech. **197**, 41–47 (2013).
[30] H. Schlichting and K. Gersten, *Boundary-Layer Theory*, 8th ed. (Springer, New Delhi, India, 2004).
[31] G. K. Batchelor, *An Introduction to Fluid Dynamics* (Cambridge University Press India Pvt. Ltd., New Delhi, India, 2009).
[32] O. Turan, N. Chakraborty, and R. J. Poole, "Laminar natural convection of Bingham fluids in a square enclosure with differentially heated side walls," J. Non-Newtonian Fluid Mech. **165**, 901–913 (2010).
[33] B. E. Launder and B. I. Sharma, "Application of the energy-dissipation model of turbulence to the calculation of flow near a spinning disc," Lett. Heat Mass Transfer **1**(2), 131–137 (1974).
[34] Fluent 6.3 User's Guide 2006 Fluent, Inc., Central Source Park, 10 Cavendish Court, Lebanon, NH 03766, USA.
[35] E. J. O'Donovan and R. I. Tanner, "Numerical study of the Bingham squeeze film problem," J. Non-Newtonian Fluid Mech. **15**, 75–83 (1984).
[36] I. A. Frigaard and C. Nouar, "On the usage of viscosity regularisation methods for visco-plastic fluid flow computation," J. Non-Newtonian Fluid Mech. **127**(1), 1–26 (2005).
[37] M. Chatzimina, G. C. Georgiou, I. Argyropaidas, E. Mitsoulis, and R. R. Huilgol, "Cessation of Couette and Poiseuille flows of a Bingham plastic and finite stopping times," J. Non-Newtonian Fluid Mech. **129**, 117–127 (2005).
[38] W. H. Herschel and R. Bulkley, "Konsistenzmessungen von Gummi-Benzollösungen," Kolloid Z. **39**, 291–300 (1926).
[39] J. M. Owen and R. H. Rogers, *Flow and Heat Transfer in Rotating Disc Systems, Vol. 1, Rotor-Stator Systems* (Research Studies Press, Taunton, UK, 1989).
[40] B. Bradie, *A Friendly Introduction to Numerical Analysis* (Pearson Education, New Delhi, India, 2007).

This article is copyrighted as indicated in the article. Reuse of AIP content is subject to the terms at: http://scitation.aip.org/termsconditions. Downloaded to IP: 203.110.246.23 On: Sun, 10 Jan 2016 14:27:14